Journal of Computational Physics 230 (2011) 5178–5198

Contents lists available at ScienceDirect

Journal of Computational Physics

journal homepage: www.elsevier.com/locate/jcp

Multi-physics design of microvascular materials for active cooling applications

Alejandro M. Aragón [a,c], Kyle J. Smith [b], Philippe H. Geubelle [b,c,*], Scott R. White [b,c]

[a] Civil and Environmental Engineering Department, University of Illinois, 205 North Mathews Avenue, Urbana, IL 61801, USA
[b] Aerospace Engineering Department, University of Illinois, 104 South Wright Street, Urbana, IL 61801, USA
[c] Beckman Institute of Advanced Science and Technology, University of Illinois, 405 North Mathews Avenue, Urbana, IL 61801, USA

ARTICLE INFO

Article history:
Received 7 October 2010
Received in revised form 2 March 2011
Accepted 3 March 2011
Available online 21 March 2011

Keywords:
Microvascular materials
Active cooling
Multi-physics optimization
Multi-Objective Genetic Algorithms

ABSTRACT

This paper describes a framework for the design of microvascular polymeric components for active cooling applications. The design of the embedded networks involves complex and competing objectives that are associated with various physical processes. The optimization tool includes a PDE solver based on advanced finite element techniques coupled to a multi-objective constrained genetic algorithm. The resulting Pareto-optimal fronts are investigated in the optimization of these materials for void volume fraction, flow efficiency, maximum temperature, and surface convection objective functions.

1. Introduction

Numerous examples of vascular systems can be found in nature, e.g. in plants, animals and in the human body. Aside from transporting the nutrients and other necessary substances, the vascular system plays a fundamental role in thermoregulation [1], a fact widely studied in animals such as reptiles [2,3]. In the human body, the heat produced by exercise is convected through the blood to the skin to be eliminated through evaporative cooling [4,5]. Nature has served as a source of inspiration for the creation of structures and materials throughout history [6–9]. Over the past decade, polymeric materials with embedded microvascular networks have been envisioned for mimicking the self-healing capability found in living organisms [10], and repeated healing on a polymer specimen using the aid of a three-dimensional microvascular network to supply the healing agent has been demonstrated [11]. These materials are currently being investigated for thermal regulation [12]. Due to the large surface to volume ratio of microchannels, microvascular cooling has been investigated for the cooling of integrated circuits and silicon computer chips [13–15], and micro-miniature refrigerators [16].

Microvascular polymeric materials are created by extruding a fugitive ink over a polymeric substrate, with tip diameters ranging from a few microns to hundreds of microns [10]. The resulting ink scaffold is then infiltrated with liquid polymer, until reaching the desired thickness of the final sample. Once the curing process of the polymer is finished, the ink is evacuated by heating (or cooling) the system, creating the void space that constitutes the network. The autonomic response then depends on the type of fluid used in the system. As mentioned earlier, by using a coolant as the fluid, microvascular materials can be used for active cooling applications [12]. The optimization of the topology of the microvascular network for such application encompasses a set of objectives that involve several physical phenomena. The energy that drives the flow through the network needs to be minimized in an optimal design. Moreover, for a specific configuration of thermal loads,

* Corresponding author at: Aerospace Engineering Department, University of Illinois, 104 South Wright Street, Urbana, IL 61801, USA. Tel.: +1 217 244 7648; fax: +1 217 244 0720.
E-mail address: geubelle@uiuc.edu (P.H. Geubelle).

0021-9991/$ - see front matter © 2011 Elsevier Inc. All rights reserved.
doi:10.1016/j.jcp.2011.03.012

the topology of the network needs to accommodate to the most efficient layout in order to keep the maximum temperature below a threshold value or to reduce the amount of thermal energy stored in the material. Finally, the topology also needs to be concerned with the volume of voids present in the final polymer, as this will have a direct impact on the stiffness and strength properties of the resulting system.

Several approaches have been used in the optimization of flow networks, and they can be grouped into three main categories: (i) semi-analytical approaches; (ii) gradient-based search methods; and (iii) evolutionary algorithms. Within semi-analytical methods, constructal theory [17–19] gives a practical alternative for the optimization of simple problems when there is information about optimal network configurations. As the complexity of the problem increases, the knowledge about optimal configurations decreases and so does the effectiveness of this approach. The use of constructal theory in the context of microvascular materials for active cooling can be found in [20–22]. The most common methodology within gradient-based search techniques, topology optimization, is applicable for problems for which the optimization process is concerned with continuous variables and the gradient computation is straightforward. As any gradient-based search technique, the algorithm usually converges to a local optimum. In order to find the global optimum, numerous attempts with different starting configurations are often needed, and even then the extremum is not guaranteed to be the global one. The use of topology optimization in the context of flow network design is discussed in [23–25]. Evolutionary algorithms are population-based algorithms, where a randomly generated set of candidate solutions evolves towards optimal structures throughout the optimization process. Genetic algorithms (GAs), the most widely known methodology in this category, use *selection*, *crossover* and *mutation* as genetic operators. At each generation of the evolution process, the worst candidates are unlikely to be selected for reproduction, thereby mimicking Darwin's *natural selection*. Selected individuals produce a new generation of candidate solutions by interchanging information, i.e. by applying the crossover operator. These new candidates then incur slight modifications in their structures through the mutation operator. Genetic algorithms do not have the drawbacks that the other methods have as they do not require any knowledge about optimal solutions, there is no need of a gradient computation, they search the entire decision space and they can be used for both continuous- and discrete-variable problems. Nevertheless, GAs are computationally demanding, often requiring millions of individual evaluations throughout their evolution. Fortunately, the evaluation step of the GA is *embarrassingly parallel*, which means that the candidate solutions can be evaluated independently in different processes, and thus GAs can obtain close to ideal speed-ups when running in distributed-memory computers. For a thorough discussion of GAs, we refer the reader to [26,27]. Also, the reader is referred to [28] for an early example of the use of GAs for the optimization of engineering problems.

A Multi-Objective Genetic Algorithm (MOGA) is usually chosen as the underlying optimization framework when dealing with multiple objective functions. The selection mechanism in a MOGA takes into account all objectives simultaneously and determines the best candidate solutions using the concept of *Pareto optimality*: when comparing two candidate solutions, the best candidate is better in at least one objective while not being worse in the other objectives. A thorough study comparing the performance of several MOGAs is presented in [29], and their application to the optimization of micro-fluidic devices can be found in [30]. The MOGA chosen for this work is the Non-dominated Sorting Genetic Algorithm II (NSGA-II) introduced by Deb et al. [31], and a discussion on its use in the optimization of microvascular flow networks has been presented in [32]. A space of constraints was built into the original algorithm so that any number of constraints could be used in conjunction with the objective functions. In this sense, individuals are first selected according to their feasibility in the constraint function space, and if a decision cannot be made, the objective function space is analyzed next. The resulting algorithm provides a powerful tool for multi-objective constrained optimization, which can be used with an arbitrary number of objective functions and constraints. Moreover, analyzing a problem in two or three dimensions depends only on the microvascular network chosen as a template in the beginning of the optimization process. More details can be found in [32,31] and the references therein.

For difficult problems, GAs usually involve thousands of individual evaluations to obtain good candidate solutions. As a result, the cost of the algorithm is directly proportional to the cost of evaluating the objective functions involved. By optimizing objective functions that describe different physical phenomena, this tool can be used to analyze truly multi-physics problems. This paper summarizes the authors' attempt to extend the results presented in [32] to include the thermal response of the embedded network so that optimized 2D structures can be obtained in the context of active cooling applications. The temperature field can be determined by solving the corresponding partial differential equations in both fluid and solid domains. In the literature, this problem is referred to as the *conjugate heat transfer problem* [14,15]. To reduce the computational cost of the conjugate problem, we adopt in this work some simplifying assumptions that take advantage of the laminar regime of the flow and the high aspect ratio of the microchannels.

This paper is organized as follows: Section 2 discusses the mathematical representation of microvascular networks and states the network optimization problem. Section 3 describes the desired features for actively-cooled materials and introduces the objective functions and constraints considered in the optimization. Using a manufactured solution, the thermal solver is verified in Section 4. Section 5 gives a brief overview on the multi-objective constrained genetic algorithm used as the underlying optimization tool while various optimization examples are presented in Section 6.

2. Microvascular network representation

Within a polymeric component, there is an infinite number of possible network configurations, so the computational design requires considering only a finite number of them. We define as the optimization *network template* a microvascular net-

work having all possible microchannel locations for the optimization being carried. This network is represented mathematically by a graph $\mathcal{G} := (\mathcal{V}, \mathcal{E})$, where each vertex $v \in \mathcal{V}$ represents the endpoint of one or more edges in the set $\mathcal{E}$, and each edge $e \in \mathcal{E}$ represents a microchannel of the network. Thus, for each $v \in \mathcal{V}$, there exists a physical coordinate $\mathbf{x}_v \subset \Omega \subset \mathbb{R}^2$, where Ω represents the matrix of the polymeric component. Other properties can be assigned to the vertices in the graph. For example, the pressure at a vertex $v \in \mathcal{V}$ is defined as a function $p_v : v(\mathcal{V}) \to \mathbb{R}$. Similarly, properties are associated with the edges of the graph, thus $D_e : e(\mathcal{E}) \to \mathbb{R}$ and $L_e : e(\mathcal{E}) \to \mathbb{R}$ denote the diameter and the length of an edge e, respectively. The distribution of the vertices within Ω can be done arbitrarily, but it is convenient to place them over a lattice layout $\Lambda := \left\{\sum_{i=1}^{2} z_i \mathbf{e}_i | z_i \in \mathbb{Z}\right\}, \Lambda \subset \Omega$, where $\mathbf{e}_i$ represent a basis of $\mathbb{R}^2$.

Consider the set of k discrete diameters $\mathcal{D} := \{D_i\}_{i=1}^{k}$, taken from the set of possible diameter tips used in the manufacturing process of the microvascular networks [10]. The objective of the optimization process is to find the optimal values of the diameter of all microchannel segments (i.e. of the set $\mathcal{E}$ of edges defining the template on which the optimal network is to be defined) to optimize various objective functions that characterize the performance of the network, within some constraints. These objective functions and constraints, which include quantities such as thermal and flow efficiency, are described in the next section. It is important to note that, since the k possible values of the diameter of a microchannel include zero (in which case the corresponding microchannel is absent from the network), the optimal network to be computed can morph in topology. In other words, considering the zero-diameter case makes possible the evaluation of a finite number of subgraphs $\mathcal{G}' := (\mathcal{V}', \mathcal{E}')$ of the graph $\mathcal{G}$ that represents the network template, where $\mathcal{V}' \subseteq \mathcal{V}$ and $\mathcal{E}' \subseteq \mathcal{E}$. These definitions imply that, for a subgraph $\mathcal{G}'$, the *degree* $\deg(v')$ of a vertex representing the number of edges to which the vertex $v' \in \mathcal{V}'$ is connected, may not be the same as the degree for the corresponding vertex in the graph $\mathcal{G}$ of the network template (i.e. $\deg(v' \in \mathcal{V}') \leqslant \deg(v \in \mathcal{V})$). This fact has implications on the coverage of the network, as described in the following section. For now, let us borrow the following definitions from graph theory: the *minimum degree* of a graph $\mathcal{G}$, denoted $\delta(\mathcal{G})$, is defined as the minimum degree of its vertices (i.e. $\delta(\mathcal{G}) = \min_i \deg(v_i), \forall v_i \in \mathcal{V}(\mathcal{G})$); a graph $\mathcal{G}$ is *connected* if there exists a path for every pair of distinct vertices $v_i, v_j \in \mathcal{V}(\mathcal{G})$ through the existing edges of the graph $\mathcal{E}(\mathcal{G})$; finally, a *disconnected graph* $\mathcal{G}$ has at least two *connected components*, where each one of these components is a connected subgraph $\mathcal{G}'$ as defined earlier.

The optimization process then consists in assigning a diameter D_e, from the set $\mathcal{D}$ defined above, to all edges $e \in \mathcal{E}$ of the network template in order to optimize a set of objective functions $\Phi = \{\phi_i\}_{i=1}^{m}$, subject to a set of constraints $\Psi = \{\psi_i\}_{i=1}^{n}$. Note that the maximum number of possible networks configurations that can be evaluated is $k^{|\mathcal{E}|}$, where $|\mathcal{E}|$ is the number of edges in the set $\mathcal{E}$.

3. Design objectives and constraints

The design of microvascular polymeric materials is inherently an intricate process, for an ideal system must achieve several objectives. For example, it is desired that the microvascular network be *minimally invasive*, for the void of the network reduces the stiffness and strength properties of the resulting polymer. A desired feature might also be that the microvascular network distributes the fluid to all relevant parts of the matrix, thus providing *maximum coverage*. Furthermore, it might be desired that the topology of the final network design provides some degree of *redundancy*, so that the fluid can still reach all areas of the specimen even if damage or blockage occurs in certain parts of the network. It is also important that the energy needed to drive the flow through the microvascular network be minimized in an optimal design, thus *flow efficiency* is a required feature in these systems. Finally, in the context of active cooling applications, the structure of the network must be such that the *thermal energy* stored or the *maximum temperature* in the matrix are minimized for a given set of thermal loads. Intuitively, some of the design objectives discussed conflict with one another, so the optimization tool to be used needs to be able to optimize all objectives simultaneously, capturing the trade-offs between competing objectives. The following sections provide a mathematical representation of the objective functions of interest in the present study.

3.1. Flow efficiency

Microvascular networks are typically composed of microchannels with circular cross-sections and high aspect ratios (i.e. length to diameter ratio). Even in 3D scaffolds, aspect ratios of 6.25 have been reported [33]. Furthermore, due to the small diameter sizes and relatively small flow rates, the flow in these structures is laminar with a Reynolds number $Re < 1000$, a value which lies well below the onset of turbulent transition reported for these networks [34]. Fig. 1 shows a schematic of the mathematical model used to represent a biomimetic microvascular material, defined over the domain $\Omega \subset \mathbb{R}^2$. The microvascular network template, denoted $\mathcal{G}$ on the figure, contains a single inflow vertex and a single outflow. More generally, let the network inlets be represented by the set of vertices $\mathcal{S} \subset \mathcal{V}(\mathcal{G})$ and the set of outlets by the vertex set $\mathcal{T} \subset \mathcal{V}(\mathcal{G})$. Then, $\dot{m}_{\mathcal{S}} := \sum_{v \in \mathcal{S}} \dot{m}_v$ and $\dot{m}_{\mathcal{T}} := \sum_{v \in \mathcal{T}} \dot{m}_v$ are the total mass flow rate entering and leaving the polymeric component, respectively, with $\dot{m}_{\mathcal{S}} = \dot{m}_{\mathcal{T}}$. An inset of the microchannel e shows the local coordinate system $\boldsymbol{\xi}_e = (\xi_e, \eta_e)$, and the flow velocity vector $\mathbf{v}_e(\boldsymbol{\xi}_e)$. Considering a fully developed flow of constant density ρ_f, the velocity vector in microchannel e of diameter D_e and constant cross-section $A_e = \pi D_e^2/4$ is given by

$$\mathbf{v}_e(\boldsymbol{\xi}_e) = 2\bar{v}_e\left(1 - 4\frac{\eta_e^2}{D_e^2}\right)\mathbf{e}_{\xi_e}, \tag{1}$$

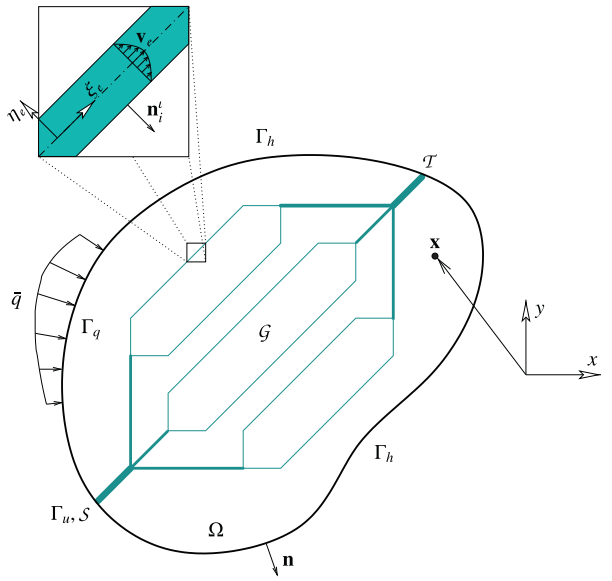

Fig. 1. Mathematical model of a biomimetic active cooling material. The material, defined over the domain $\Omega \subset \mathbb{R}^2$ with outward unit normal $\mathbf{n}$, has an embedded microvascular network, represented by a graph data structure $\mathcal{G}$. The domain contains an inflow $\mathcal{S}$ and an outflow $\mathcal{T}$. The total mass flow rate entering the material is $\dot{m}_{\mathcal{S}}$. An inset of microchannel e shows the velocity profile $\mathbf{v}_e(\xi_e)$ assuming laminar flow. For the thermal boundary value problem, the boundary of the domain is split in mutually exclusive regions Γ_u, Γ_q and Γ_h, where Dirichlet, Neumann, and Robin boundary conditions are applied, respectively.

where $\bar{v}_e$ is the mean velocity defined such that $\dot{m}_e \equiv \rho_f \bar{v}_e A_e$, with $\dot{m}_e$ denoting the mass flow rate in the channel. Then, the pressure drop between the end-vertices $v_j, v_k, \in \mathcal{V}$ of the channel is obtained using the Hagen–Poiseuille law,

$$\Delta p_e = \frac{128 \nu L_e}{\pi D_e^4} \dot{m}_e, \tag{2}$$

where ν denotes the kinematic viscosity of the fluid. The assumption of fully developed flow is valid everywhere but close to inlet locations and microchannel junctions. The hydrodynamic entry length can be estimated [35] by

$$\xi_h \approx 0.05 D_e Re. \tag{3}$$

For the aspect ratios considered, the ratio $\xi_h / L_e = 0.005 Re$ is very small so the flow can be considered as fully developed throughout the channel. Eq. 2 can be rearranged to express the mass flow rate contribution at the end-vertices of the channel:

$$\begin{Bmatrix} \dot{m}_{v_j} \\ \dot{m}_{v_k} \end{Bmatrix} = \frac{\pi D_e^4}{128 \nu L_e} \begin{bmatrix} 1 & -1 \\ -1 & 1 \end{bmatrix} \begin{Bmatrix} p_{v_j} \\ p_{v_k} \end{Bmatrix}. \tag{4}$$

More generally, the formulae above are also valid for the subgraphs of the microvascular network template, i.e. $\mathcal{G}' \subseteq \mathcal{G}$. Considering the contribution of $|\mathcal{E}'|$ microchannels, a system of linear equations $\vec{K}\vec{p} = \vec{m}$ is assembled, where $\vec{K}$ is the network characteristic matrix of size $|\mathcal{V}'| \times |\mathcal{V}'|$, $\vec{p}$ the pressure vector and $\vec{m}$ the mass flow rate vector [36]. Two types of boundary conditions are considered when solving this system of equations. The mass flow rate is prescribed over the vertex set $\mathcal{S} \subset \mathcal{V}'$, that represents network inlets, while network outlets, represented by the vertex set $\mathcal{T} \subset \mathcal{V}'$, have prescribed pressure values. Prescribed pressure values are typically set at zero, so that the computed pressure value at each network vertex corresponds to the difference with the outflow pressure. The pressure distribution in the network is fully determined after solving this system of linear equations.

Let us define the flow efficiency objective function $\phi_f : \mathcal{V}'(\mathcal{G}') \to \mathbb{R}$ as

$$\phi_f := \max_{v'_i, v'_j \in \mathcal{V}'} \left| p_{v'_i} - p_{v'_j} \right|. \tag{5}$$

In other words, the maximum pressure difference in the microvascular network represented by the subgraph $\mathcal{G}' = (\mathcal{V}', \mathcal{E}')$ can be used to quantitatively describe the amount of energy needed to drive the flow through the network. The flow in each channel can also be computed once the pressure distribution is obtained by using Eq. 2.

Eq. 5 can be applied in two different contexts. The first one considers a constant value of the total mass inflow rate $\dot{m}_{\mathcal{S}}$. This case is straightforward and the objective function is obtained directly after solving the system of linear equations mentioned above. The second context considers a constant power

$$P := \frac{1}{\rho_f} \sum_{v \in \mathcal{S}} \dot{m}_v p_v, \tag{6}$$

where p_v represents the pressure at inlet locations (i.e. $v \in \mathcal{S}$) in excess of the value prescribed at outlet locations. In this case, the prescribed mass flow rates are scaled such that the power P remains constant for each network. In other words, instead of considering a constant mass inflow throughout the optimization, the power is fixed to the value of the template configuration P^0. The power P is computed for each individual after solving for the flow efficiency objective function using the initial flow boundary conditions, and a scaling factor is obtained as the ratio between the reference power P^0 and P. This factor is used to scale both the pressure and the mass flow rate, such that the power of the candidate solution equals that of the template configuration P^0.

3.2. Void volume fraction

As described previously, the microvascular network may have a detrimental impact on the stiffness and strength properties of the resulting polymer. To achieve a minimally invasive network, we aim to minimize the network void volume fraction objective function $\phi_v : \mathcal{E}'(\mathcal{G}') \to \mathbb{R}$, defined as

$$\phi_v := \frac{\sum_{e' \in \mathcal{E}'} L_{e'} D_{e'}}{A_\Omega}, \tag{7}$$

i.e. as the projected area of microchannels normalized by the area of the domain A_Ω. During the optimization process, groups of channels with no pressure differential (and therefore no flow) are eliminated prior to the computation of ϕ_v.

3.3. Thermal field

For the definition of the thermal boundary value problem, we refer again to Fig. 1. The domain that represents the material $\overline{\Omega} \subset \mathbb{R}^2$ is defined such that $\overline{\Omega} := \overline{\Omega_s \cup \Omega_f}$, where Ω_s and Ω_f represent mutually exclusive parts of the domain occupied by the solid and the fluid, respectively. The boundary of the domain $\Gamma := \overline{\Omega} - \Omega$, with outward unit normal $\mathbf{n}$, is partitioned into regions Γ_u, Γ_q and Γ_h, where Dirichlet, Neumann and Robin boundary conditions are applied, respectively. The boundary regions are also mutually exclusive such that $\Gamma = \overline{\Gamma_u \cup \Gamma_q \cup \Gamma_h}$ and $\Gamma_u \cap \Gamma_q \cap \Gamma_h = \emptyset$. Finally, there are $|\mathcal{E}'|$ interfaces between the fluid and the solid domains, defined as $\mathcal{I} = \{\imath_i\}_{i=1}^{|\mathcal{E}'|} := \overline{\Omega_s \cap \Omega_f} \setminus \Gamma$, each one with normal vector $\mathbf{n}_i^\imath$.

The temperature distribution in the mathematical representation of the microvascular polymeric material can then be obtained by solving the conjugate heat transfer boundary value problem. This implies solving for the temperature in both solid and fluid domains, subject to a set of boundary conditions and ensuring continuity of the temperature and heat flux along solid–fluid interfaces. This requires a discretization in both domains and the exchange of information between them if a non-monolithic solver is used. To reduce the problem size, we adopt the following expression of the heat flow rate per unit length q_e at channel e, which can be obtained through an energy balance [37]:

$$q_e = \dot{m}_e c_p \frac{du}{d\xi_e}, \tag{8}$$

with c_p denoting the specific heat of the fluid, and $du/d\xi_e$ representing the gradient of the temperature in the direction of the channel. This equation assumes a fully developed temperature profile and also constant heat rate along the wall of the channel. The small diameters (of the order of tens to hundreds of microns) and the high aspect ratios of these microchannels allow us to mathematically treat them as line segments. Then, the simplified equation for the heat flow rate given by Eq. 8 allows us to consider the cooling effect of the microchannels as heat sources (or sinks) over these line segments, without the need to solve explicitly for the temperature in the fluid. The strong form of the simplified thermal problem becomes: Given the density ρ_f and specific heat c_p of the fluid, the ambient fluid temperature u_∞, the heat transfer coefficient $h : \Gamma_h \to \mathbb{R}$, the thermal conductivity tensor in the solid $\boldsymbol{\kappa} : \overline{\Omega} \to \mathbb{R}^2 \times \mathbb{R}^2$, the heat source $f : \Omega \to \mathbb{R}$, prescribed temperature $\bar{u} : \Gamma_u \to \mathbb{R}$ and prescribed heat flux $\bar{q} : \Gamma_q \to \mathbb{R}$, find the temperature field in the solid u such that

$$\nabla \cdot (\boldsymbol{\kappa} \nabla u) + f = \delta(\mathbf{x} - \mathbf{x}_e) c_p \dot{\mathbf{m}}_e \cdot \nabla u \quad \text{on } \Omega, \tag{9}$$

with $\dot{\mathbf{m}}_e = \dot{m}_e \mathbf{e}_{\xi_e}$, and boundary conditions

$$u = \bar{u} \quad \text{on } \Gamma_u, \tag{10}$$

$$\boldsymbol{\kappa} \nabla u \cdot \mathbf{n} = \bar{q} \quad \text{on } \Gamma_q, \tag{11}$$

$$\boldsymbol{\kappa} \nabla u \cdot \mathbf{n} = h(u_\infty - u) \quad \text{on } \Gamma_h, \tag{12}$$

where the Dirac delta function is introduced to represent the location of the microchannels in the 2D domain. The boundary value problem given by Eqs. (9)–(12) is solved using a finite element formulation, as described in Section 4.

The maximum temperature objective function $\phi_T : \Omega^h \to \mathbb{R}$ is defined as

$$\phi_T := \max u^h(\mathbf{x}), \quad \forall \mathbf{x} \in \Omega^h, \tag{13}$$

where Ω^h is a finite element discretization of Ω and u^h is an approximate solution of u obtained from a discrete formulation.

In most applications, the source term f in Eq. 9 is zero. However, there is a class of problems for which the 2D domain represents a microvascular fin surrounded by a fluid at temperature u_∞. In that case, the source term takes the form $f = h_f(u_\infty - u)$, where h_f denotes the film coefficient describing the heat transfer between the fin and its surrounding. For this class of design problems, we introduce the surface convected energy objective function $\phi_s : \Omega^h \to \mathbb{R}$ as

$$\phi_s := \frac{1}{\Omega^h} \sum_{\alpha=1}^{M} \int_{\Omega_\alpha} h_f(u^h(\mathbf{x}) - u_\infty) d\Omega. \tag{14}$$

where M denotes the number of elements that discretize Ω^h.

3.4. Connectivity constraint

The objective functions introduced above are computed only for connected graphs. When the candidate solutions are allowed to morph in structure throughout the optimization process, many of the subgraphs $\mathcal{G}' := (\mathcal{V}', \mathcal{E}')$, of the graph $\mathcal{G}$ that represents the network template become unfeasible because $\mathcal{G}'$ is not a connected graph. In this case the candidate solution is marked as unfeasible. A very simple constraint can be obtained as

$$\psi_c := \begin{cases} 1 & \text{if } \mathcal{G}' \text{ is disconnected,} \\ 0 & \text{otherwise.} \end{cases}$$

However, this simple constraint is modified in practice so that it is easier to move away from the unfeasibility region. A better constraints relies on the number of connected components of the subgraph:

$$\psi_c := c(\mathcal{G}') - 1,$$

where the function $c : \mathcal{G}' \to \mathbb{Z}$ gives the number of connected components. Finally, the number of edges in the subgraph can be used to move away from the unfeasibility region, considering the fact that the template network, which contains the maximum possible number of edges, is feasible:

$$\psi_c := \begin{cases} 1/|\mathcal{E}'(\mathcal{G}')| & \text{if } \mathcal{G}' \text{ is disconnected,} \\ 0 & \text{otherwise.} \end{cases} \tag{15}$$

Eq. 15 is used to impose the connectivity constraint in all optimization examples studied in this work.

4. Thermal solver

For the weak formulation, let $\mathcal{U} = \{u | u|_{\Gamma_u} = \bar{u}\} \subset H^1(\overline{\Omega})$ be the set of trial solutions for the temperature field and $\mathcal{V} = \{v | v|_{\Gamma_u} = 0\} \subset H^1_0(\overline{\Omega})$ be the variation space. The weak form of the problem is: Given ρ_f, c_p, u_∞, h, $\boldsymbol{\kappa}$, f, $\bar{q}$, $\bar{u}$ as defined earlier in Section 3.3, find $u \in \mathcal{U}$ such that

$$a(w,u) + a(w,u)_{\Gamma_h} = (w,f) + (w,\bar{q})_{\Gamma_q} + (w,u_\infty)_{\Gamma_h} \quad \forall w \in \mathcal{V}, \tag{16}$$

where the bilinear and linear forms are given by

$$a(w,u) = \int_\Omega (\nabla w \cdot (\boldsymbol{\kappa} \nabla u) + w\delta(\mathbf{x} - \mathbf{x}_e) c_p \dot{\mathbf{m}}_e \cdot \nabla u) d\Omega, \tag{17}$$

$$a(w,u)_{\Gamma_h} = \int_{\Gamma_h} whu \, d\Gamma, \tag{18}$$

$$(w,f) = \int_\Omega wf \, d\Omega, \tag{19}$$

$$(w,\bar{q})_{\Gamma_q} = \int_{\Gamma_q} w\bar{q} \, d\Gamma, \tag{20}$$

$$(w,u_\infty)_{\Gamma_h} = \int_{\Gamma_h} whu_\infty \, d\Gamma. \tag{21}$$

Eq. 16 is discretized using a finite element formulation. It is worth noting that the resulting matrix in the discrete form is not symmetric due to the convective term in the bilinear form of Eq. 17.

Let us partition the domain in M finite elements with a total of N nodes such that $\Omega^h \equiv \text{int}(\cup_{\alpha=1}^{M} \overline{\Omega}_\alpha) \approx \Omega$. A more advanced framework can be used to obtain the temperature field. The Generalized Finite Element Method (GFEM) enables us to obtain the temperature field in finite element meshes that are completely independent of the geometry of the microvascular networks. Because the topology of the optimal network is not known a priori, it is desirable that the finite element mesh used to solve the thermal field be completely independent of the location of the microchannels. Enrichment functions

used in the GFEM that recover optimal convergence rates, developed especially for this work, have been proposed by the authors in [38]. In the GFEM framework, the temperature field approximation becomes

$$u^h(\mathbf{x}) = \sum_{\alpha=1}^{N} \varphi_\alpha(\mathbf{x})\widetilde{U}_\alpha + \sum_{\alpha=1}^{N} \varphi_\alpha(\mathbf{x}) \sum_{i=1}^{E} L_{\alpha i}(\mathbf{x})\widehat{U}_{\alpha i}, \tag{22}$$

where the first term corresponds to the standard finite element interpolation (with standard degrees of freedom $\widetilde{U}_\alpha$), the second term to the enriched/extended part of the approximation (with enrichment degrees of freedom $\widehat{U}_{\alpha i}$), and the functions $\{L_{\alpha i}(\mathbf{x}) : \omega_\alpha \to \mathbb{R}\}_{i=1}^{E}$, with $\omega_\alpha := \{\mathbf{x} | \varphi_\alpha(\mathbf{x}) \neq 0\}$ being the *cloud* or *support* of $\mathbf{x}_\alpha$, attempt at capturing some *a priori* information about the solution of a problem. See also [39] for more details on the GFEM.

For the discussion that follows, polynomial and ramp enrichment functions [38] are used for the GFEM:

$$\mathcal{L} = \{1, \xi, \eta\} \times \{1, r_i\}_{i=1}^{2}, \tag{23}$$
$$\xi = \frac{x - x_\alpha}{h_\alpha}, \quad \eta = \frac{y - y_\alpha}{h_\alpha},$$

where (x_α, y_α) are the coordinates of the node $\mathbf{x}_\alpha$, h_α is a scaling parameter that is proportional to the size of the cloud or support of node $\mathbf{x}_\alpha$, and r_i are the ramp functions described in [38]. This choice of enrichments results in an approximation that recovers optimal quadratic convergence.

A manufactured solution is constructed to verify the implementation of the weak formulation given by Eq. 16. Consider the domain $\Omega = L_x \times L_y$ shown in Fig. 2(a).

Assume that along the line $y = \alpha L_y$, with $0 < \alpha < 1$, heat is being generated in proportion to the x-derivative (i.e. $f_1 = C\partial u/\partial x$, with C constant), following the reasoning behind Eq. 8. Thus, along that line, the jump in the heat flux equals the generated heat:

$$\kappa [\![\frac{\partial u}{\partial y}]\!]_{y=\alpha L_y} = C \frac{\partial u}{\partial x}\bigg|_{y=\alpha L_y}.$$

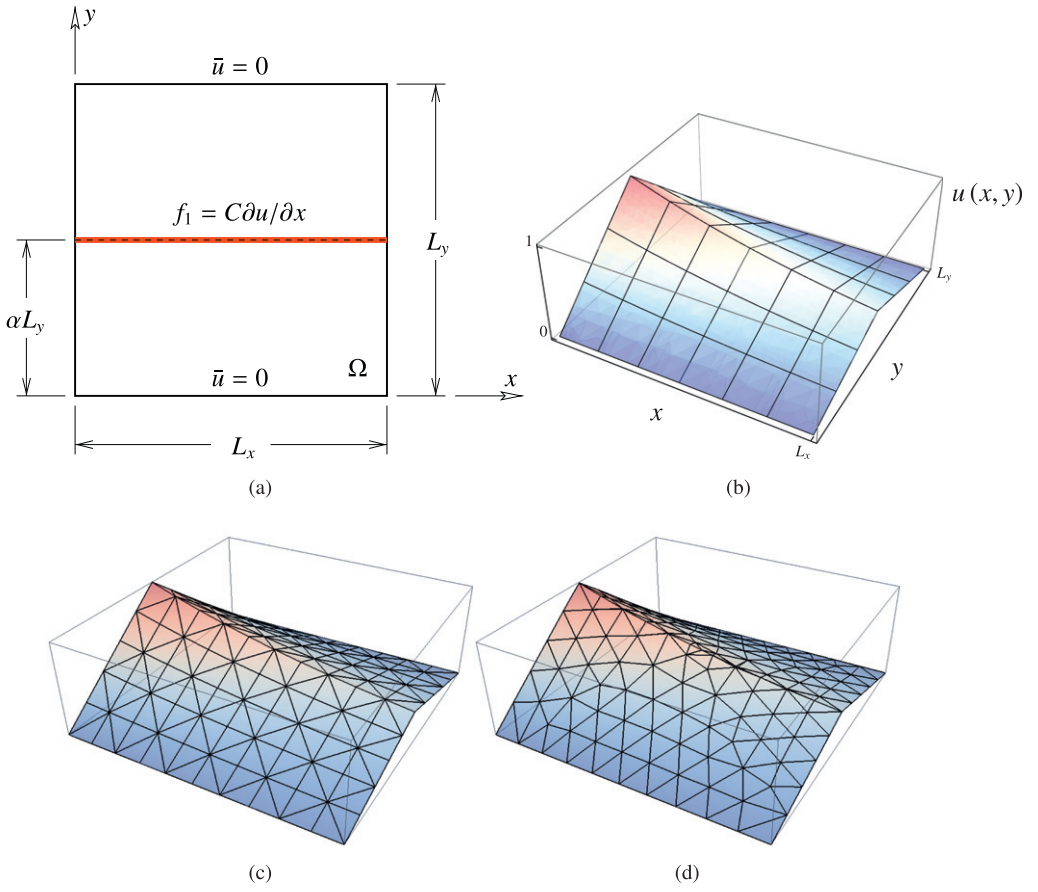

Fig. 2. Manufactured solution. (a) Schematic of the domain used, showing a heat source f_1 proportional to the x-derivative. (b) Exact temperature distribution given by Eq. 24. (c) Finite element approximation on a matching mesh of 3-node triangular elements. (d) Generalized finite element quadratic approximation on a non-matching mesh of 3-node triangular elements using $\{1, \xi, \eta\} \times \{1, r_i\}_{i=1}^{2}$ as enrichment functions.

It can be shown that a temperature satisfying the equation above can be written as

$$u(x,y) = e^{-\kappa x/C\alpha L_y(1-\alpha)}\left[\frac{y}{\alpha L_y} - \frac{y-\alpha L_y}{\alpha(1-\alpha)L_y}\mathcal{H}(y-\alpha L_y)\right], \tag{24}$$

where $\mathcal{H}(\cdot)$ is the Heaviside step function. Substituting Eq. 24 into the heat equation gives the form of the heat source f needed to satisfy the equation.

The temperature field of Eq. 24 is illustrated in Fig. 2(b) for $\alpha = 0.5$. Approximate solutions are also given in Fig. 2(b) and (c) for a matching and a non-matching mesh, respectively.

In the matching case, a finite element mesh of 3-node triangles is used, where the edges of the elements follow the heat source applied along the line. For the non-matching case, the generalized finite element method is used, with a quadratic approximation given by the use of the enrichment functions in Eq. 23. A mesh of 3-node triangles is used as the underlying mesh, hence with a linear *partition of unity*.

5. Genetic algorithms

With the formulation of the objective functions and constraints at hand, we now turn to the underlying optimization methodology. Genetic algorithms have been chosen for this work for a number of reasons. First, GAs do not require any *a priori* knowledge about optimal solutions. However, such knowledge can be exploited by creating a better starting guess for the population of individuals. The encoding of the problem gives powerful flexibility so the method can be used to solve both continuous- and discrete-variable problems. As mentioned earlier, GAs can be combined with a Pareto-selection mechanism to create Multi-Objective Genetic Algorithms (MOGAs). In these algorithms, individuals evolve all objectives simultaneously and the end result is usually a Pareto-optimal front of individuals, where all candidates are optimal solutions to the multi-objective optimization problem. The addition of a space of constraints creates a powerful tool for constrained multi-objective optimization, that can be used with an arbitrary number of objectives and constraints. GAs search the entire decision space so the optimal solutions found are likely to be global optima. Finally, the algorithm can be combined with other optimization procedures (e.g. gradient-based search techniques such as topology optimization or even another type of evolutionary algorithm) resulting in a *hybrid* methodology. In this regard the GA is used to search globally while the other search technique is used to find the local optimum. GAs have the disadvantage of consuming vast computational resources. However, GAs are embarrassingly parallel so a considerable speed-up can be obtained when running the algorithm in distributed-memory systems. The parallelization of GAs is challenging for problems where the evaluation time (i.e. the computational time required to evaluate objective functions and constraints) varies among individuals, requiring advanced load balancing techniques among processors. The parallelization scheme adopted in this work is discussed later in this section.

Genetic algorithms evolve a population $\mathcal{P}$ of candidate solutions, or *individuals* $\mathcal{I}$ in GA terminology. Each individual contains a *chromosome* $\mathcal{C}$, that encodes in each one of its *alleles* $\mathcal{A}$ the candidate solution. The encoding used in this study is discussed next. As explained in Section 2, the optimization starts with a microvascular network template. This network is represented by a graph $\mathcal{G} = (\mathcal{V}, \mathcal{E})$, with a total of $|\mathcal{E}|$ possible microchannels. Each chromosome that represents a candidate solution has length equal to the number of microchannels (i.e. $|\mathcal{C}| = |\mathcal{E}|$), and each of its alleles gets a value from a diameter set $\mathcal{D} = \{D_i\}_{i=1}^{k}$ that contains the possible diameter choices. In GA terminology, this is termed k-ary encoding. As explained previously, considering the zero diameter allows the network to morph in structure from the network template. The mapping resulting from applying a chromosome $\mathcal{C}$ to the graph $\mathcal{G}$ can be thought of as a function $f : \mathcal{G} \to \mathcal{G}' \subseteq \mathcal{G}$, resulting in a subgraph with fewer edges when considering the zero diameter.

The adopted multi-objective GA, outlined in Algorithm 1, is called the Non-dominated Sorting Genetic Algorithm II (or NSGA-II) and is attributed to Deb et al. [31].

Algorithm 1. Non-dominated Sorting Genetic Algorithm

procedure EVOLVE$|\mathcal{P}|, t_{\max}$
  $\mathcal{P}_0 = \text{RANDOM}(|\mathcal{P}|)$
  $Q_0 = \text{APPLYGENETICOPERATORS}(\mathcal{P}_0)$
  while $t < t_{\max}$ **do**
    $R_t = \mathcal{P}_t \cup Q_t$
    $\mathcal{F}_i = \text{FASTNONDOMINATEDSORT}(R_t)$
    repeat
      $\text{CROWDINGDISTANCEASSIGNMENT}(\mathcal{F}_i)$
      $\mathcal{P}_{t+1} = \mathcal{P}_{t+1} \cup F_i$
    until $|\mathcal{P}_{t+1}| < |\mathcal{P}|$
    $sort(\mathcal{P}_{t+1}, \lll)$
    $\mathcal{P}_{t+1} = \mathcal{P}_{t+1}[0 : |\mathcal{P}|]$
    $Q_{t+1} = \text{APPLYGENETICOPERATORS}(\mathcal{P}_{t+1})$
    $t \leftarrow t + 1$
  end while
end procedure

Given the population size $|\mathcal{P}|$, the algorithm starts by creating a random population of individuals $\mathcal{P}_0$. A children population $\mathcal{Q}_0$ is then created by applying genetic operators *selection*, *crossover* and *mutation*. Then the algorithm enters a loop over a maximum number of iterations (or *generations*) $t_{\max}$, where the initial population evolves over time towards better candidate solutions. At each generation, the combined parent–children population $\mathcal{R}_t$ is split into sets $\mathcal{F}_i$ (non-dominated fronts) according to their domination rank (see below). The population for the next generation is then obtained by considering individuals starting from the best fronts until the population size equals $|\mathcal{P}|$, considering also a *crowding distance* parameter, used to populate the resulting fronts better. The genetic operators are applied again to obtain the children population for the next generation and the process is repeated.

The original algorithm was modified in the present study in order to handle constraints by using the operator $\lll$ defined as follows: Given the objective function space Φ, an individual $\mathcal{I}_i$ that is better than (or dominates) another individual $\mathcal{I}_j$ in that space, is expressed as $\mathcal{I}_i \ll_\Phi \mathcal{I}_j$. For this to be true, the corresponding objective functions are compared and individual $\mathcal{I}_i$ is better in at least one of them while being no worse in the rest. This concept, due to Vilfredo Pareto [40], is called *dominance* and it is borrowed from the field of economics. Similarly, considering the constraint space Ψ, $\mathcal{I}_i \ll_\Psi \mathcal{I}_j$ implies that individual $\mathcal{I}_i$ dominates individual $\mathcal{I}_j$ in the constraint function space. At any generation $t < t_{\max}$, the population $\mathcal{P}$ can be split into two mutually exclusive sets (i.e. $\mathcal{P} = \mathcal{P}^F \cup \mathcal{P}^U,\ \mathcal{P}^F \cap \mathcal{P}^U = \emptyset$), where $\mathcal{P}^F$ and $\mathcal{P}^U$ contain only feasible and unfeasible individuals, respectively. The operator $\ll$ considers both spaces, so the domination of individual $\mathcal{I}_i$ over individual $\mathcal{I}_j$ is expressed as follows:

$$\mathcal{I}_i \ll \mathcal{I}_j \Longleftrightarrow \begin{cases} \mathcal{I}_i \in \mathcal{P}^F, & \mathcal{I}_j \in \mathcal{P}^U, \\ \mathcal{I}_i, \mathcal{I}_j \in \mathcal{P}^U, & \left(\mathcal{I}_i \ll_\Psi \mathcal{I}_j\right) \text{ or } \left(\mathcal{I}_i \not\ll_\Psi \mathcal{I}_j \text{ and } \mathcal{I}_i \ll_\Phi \mathcal{I}_j\right), \\ \mathcal{I}_i, \mathcal{I}_j \in \mathcal{P}^F, & \mathcal{I}_i \ll_\Phi \mathcal{I}_j. \end{cases} \tag{25}$$

This operator is also used during the selection process when the genetic operators are applied. Finally, the operator $\lll$ considers also the crowding distance assignment, so that

$$\mathcal{I}_i \lll \mathcal{I}_j \Longleftrightarrow (\mathcal{I}_i \ll \mathcal{I}_j) \text{ or } (\mathcal{I}_i \not\ll \mathcal{I}_j \text{ and } c_i > c_j), \tag{26}$$

where c_i and c_j are the crowding distance values for individuals $\mathcal{I}_i$ and $\mathcal{I}_j$, respectively [31,32]. In Eqs. (25) and (26), $(\cdot \not\ll \cdot)$ implies non-domination, e.g. $\mathcal{I}_i \not\ll_\Psi \mathcal{I}_j$ implies also $\mathcal{I}_j \not\ll_\Psi \mathcal{I}_i$.

5.1. Parallel implementation

As the size of the problem increases, the parallelization of the GA is required if a Pareto-optimal front is to be obtained in a reasonable amount of time. The following analysis follows the methodology presented by Cantú-Paz and Goldberg [41]. Let us assume a master–slave approach for the parallelization, where slave processes are in charge of the evaluation of all objective functions and constraints for the individuals they receive and the master process receives this information and applies genetic operators. Considering only the evaluation part of the GA, the total parallel computational time is

$$T_p = (p-1)t_c + \frac{\bar{t}_e|\mathcal{P}|}{p-1}, \tag{27}$$

where t_c is the communication time, $\bar{t}_e$ the average evaluation time, $|\mathcal{P}|$ is the population size and p the number of processes. The optimal number of processes to solve this problem is given by

$$p^\star = 1 + \sqrt{\gamma|\mathcal{P}|}, \tag{28}$$

with $\gamma = \bar{t}_e/t_c$. The speed-up $S_p = T_s/T_p$, defined as the ratio between sequential and parallel computational times, is then

$$S_p = \frac{\gamma|\mathcal{P}|}{(p-1) + \gamma|\mathcal{P}|/(p-1)}. \tag{29}$$

Note that the inherent part of the GA (i.e. the time spent on genetic operators and in the NSGA-II front determination) is neglected in this analysis, so Eq. 29 reflects only the speed-up in the evaluation. For the problems investigated in this work, the time spent in the inherent part of the GA can indeed be neglected and Eq. 29 gives a good estimation of the speed-up. Fig. 3 shows the speed-up S_p and efficiency $E_p = S_p/p$ as a function of p for $\gamma = \{250x\}_{x=1}^4$ and a population size $|\mathcal{P}| = 1000$. This population size is typical for the type of optimization problems studied in this work. The figures show that using an arbitrary number of processes can have a detrimental impact on the total computational time due to communication time. The speed-up figure also shows the optimal number of processes given by Eq. 28.

It is worth mentioning that for problems where the individuals can have very different computation times, a naive implementation that considers no load balancing would reduce the efficiency, as defined above. In the present study, the evaluation times for the candidate solutions vary drastically, as all objective functions can only be computed for those individuals that are feasible. The time complexity of the algorithm used to find out the number of connected components in the network of the candidate solution is $O(\mathcal{V}' + \mathcal{E}')$, and this time is spent to find out if the individual is feasible or not. When a microvascular network that is not connected is found, the individual is marked as unfeasible and no time is spent computing the

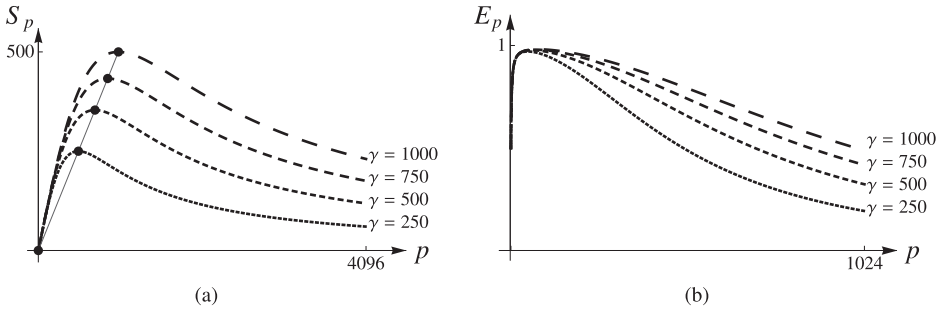

Fig. 3. (a) Speed-up $S_p = T_s/T_p$; and (b) efficiency $E_p = S_p/p$, as a function of the number of processes p for a population size $|\mathcal{P}| = 1000$ and $\gamma = \{250x\}_{x=1}^{4}$.

objective functions defined in Section 3. The objective functions studied in this work have very different time complexities. The computation of the void volume fraction ϕ_v has complexity $O(\mathcal{E}')$. For the flow efficiency objective function ϕ_f, the time complexity is $O(\mathcal{V}^3)$. Finally, the maximum temperature objective function ϕ_T and the surface convected energy objective function ϕ_s have complexity $O(N^3)$, with N being the number of nodes in the finite element mesh. Because the number of nodes in a mesh is clearly larger than the number of vertices in the network of a candidate solution, the evaluation of a feasible individual has complexity $O(N^3)$, which is much higher than that of an unfeasible individual $O(\mathcal{V}' + \mathcal{E}')$.

6. Results

As indicated earlier, a GA-based optimization of microvascular materials has been presented in [32], with emphasis on maximizing the flow efficiency and minimizing the void volume fraction of the embedded network. Here we extend that methodology to multi-physics optimization that includes the solution of the temperature field. Tournament selection, uniform crossover, and bit-wise mutation are used as genetic operators for the GA [26,27]. In the following examples, water is used as the coolant, with density $\rho_f = 1000\ \text{kg/m}^3$, kinematic viscosity $\nu = 1.05 \times 10^{-6}\ \text{m}^2/\text{s}$ and specific heat $c_p = 4185.5\ \text{J/kg K}$.

6.1. Uniform heat trap example

This first application is used primarily as a verification problem and consists of a rectangular domain $\Omega = (26 \times 12)\ \text{mm}^2$, with two holes $\omega = (7 \times 2)\ \text{mm}^2$, as represented in Fig. 4. The figure displays the microvascular network template, consisting of 446 channels. Flow boundary conditions include prescribed mass flow rate $\dot{m}_v = 10\ \text{g/min}\ \forall v \in \mathcal{S}$ of water at three locations over the left edge and prescribed zero pressure at three locations over the right edge, as shown in the figure. For the thermal boundary value problem, a uniform heat source is applied to the domain strip between the two holes. All free edges in the domain have a convective boundary condition. Fig. 4 also shows the temperature field in the absence of flow, where a maximum temperature $u_{\max} = 327\ \text{K}$ is reached. Thus, this problem tests the ability of the genetic algorithm to obtain a microvascular network configuration where the flow is collected into a single channel that passes through the central strip where the heat source is applied. Intuitively, this structure would minimize the value of ϕ_T. The optimization problem is then stated as:

$$\text{minimize } \Phi = \{\phi_v, \phi_f, \phi_T\},$$
$$\text{such that } \psi_c = 0.$$

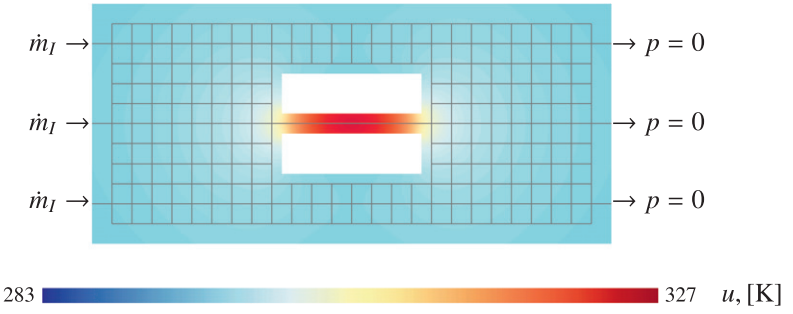

Fig. 4. Microvascular network template with 446 microchannels showing the flow boundary conditions and temperature solution in the absence of flow for the uniform heat trap example.

The diameter set used throughout the optimization is $\mathcal{D}[\mu m] = \{0, 350\}$, and the temperature of the fluid at inlet locations considered is u_f = 283.15 K. A population size $|\mathcal{P}| = 3200$ is chosen for the GA evolution. Results are reported for both constant mass inflow rate and constant power.

6.1.1. Constant inflow results

The evolution of the objective functions (normalized with those corresponding to the microvascular network template shown in Fig. 4, ϕ_v^0, ϕ_f^0 and ϕ_T^0) is illustrated in Fig. 5. The figure omits the first ten generations because they did not contain any feasible individuals (i.e. all candidate solutions contained disconnected networks). As apparent in the figure, the temperature objective function ϕ_T converges fast and remains roughly constant throughout the evolution. The other two objective functions need a higher number of generations to converge.

The entire Pareto-optimal front at generation t = 2000 is illustrated in Fig. 6. The front contains two well defined branches, as illustrated clearly in the projection of the front on the $\phi_f - \phi_T$ plane. One of the branches remains roughly constant for the value of ϕ_T, and contains individuals for which the flow is entirely collected in microchannels passing through the central strip where the uniform heat source is applied. Thus, these candidate solutions are the best for minimizing the value of the maximum temperature ϕ_T. More precisely, individuals with increasing value of ϕ_v and decreasing value of ϕ_f have a slightly higher value of ϕ_T. Therefore, the individual that minimizes the maximum temperature objective function is not flow efficient. This individual, labeled (a) and marked with a □ symbol on the Pareto-optimal front, belongs to this first branch and it is revealed in Fig. 7(a). Arrows in Fig. 7 represent the flow, so their sizes and gray scale are proportional to the flow magnitude. As expected, the flow is collected into a single microchannel. This individual not only minimizes the value of ϕ_T, but also the void volume fraction objective function ϕ_v. The other branch contains individuals where the flow is not collected entirely through the central strip, thus yielding a higher value of ϕ_T. However, individuals in this branch have a better value of the flow efficiency objective function ϕ_f because the flow is divided in multiple paths from inflow to outflow locations, which in turn increases the value of the void volume fraction ϕ_v. The individual shown in Fig. 7(b), which maximizes the flow efficiency at this particular generation, belongs to this branch and it is labeled (b) and marked with a ○ symbol on the front. The structure of this individual is very close to that of the network template, thus having a very high value of the void volume fraction objective function ϕ_v. The ranges for the objective function values for this problem are as follows: ϕ_v [%]: (2, 14), ϕ_f [MPa]: (0.8, 5.7) and ϕ_f [K]: [294.7, 313.1].

6.1.2. Constant power results

For the case of constant power, the entire front and its projections are presented in Fig. 8 at generation t = 4000, and three of its candidate solutions (marked with symbols in the front and its projections) are illustrated in Fig. 9. Note that the range of values for the flow in the latter is different from that shown in Fig. 7. There are noticeable changes on the front, when comparing it to the front for constant inflow shown in Fig. 6. The ranges for the objective functions are as follows: ϕ_v [%]: (2, 15), ϕ_f [MPa]: (0.75, 2.23) and ϕ_f [K]: [301.6, 326]. The pressure range changes drastically, reducing the upper bound considerably. However, this is just an apparent benefit because the temperature range is now considerably higher. The Pareto-optimal front is also divided in more than two branches, some of which contain just a few individuals. There is a branch that contains a single individual, the one that minimizes the void volume fraction (Fig. 9(a) and individual marked with a ◇ in the

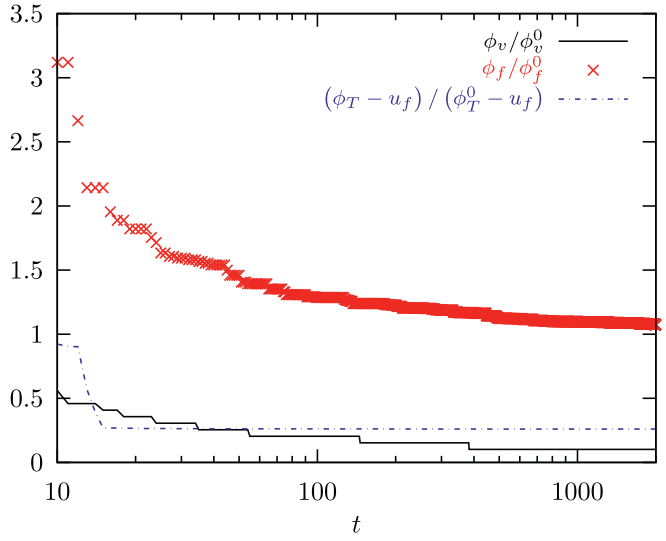

Fig. 5. Void volume fraction, flow efficiency and maximum temperature objective functions as a function of generations t for the uniform heat trap example. The objective function values are normalized with those of the microvascular template network ϕ_v^0, ϕ_f^0 and ϕ_T^0, and with the fluid temperature u_f.

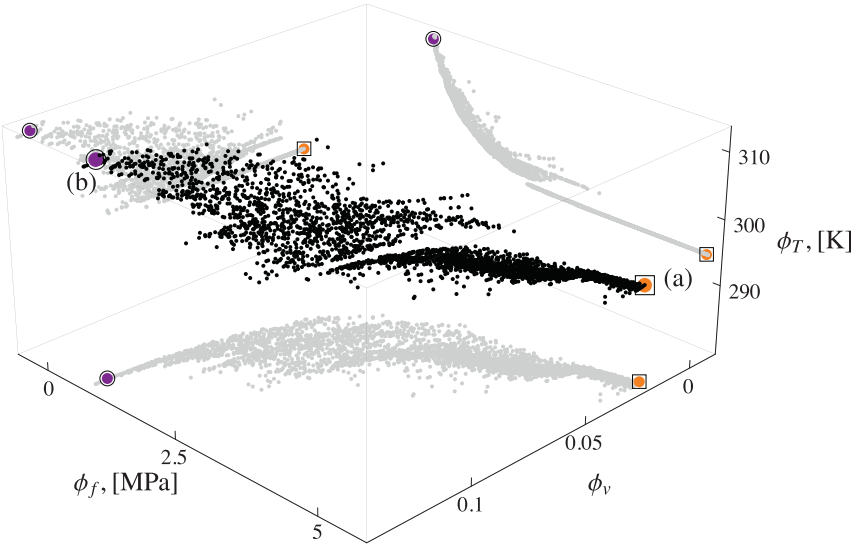

Fig. 6. Pareto-optimal front and its projection to three orthogonal planes after 2000 generations of the genetic algorithm for the uniform heat trap example under constant inflow conditions. Selected candidate solutions in the front correspond to those shown in Fig. 7(a) and (b), and are marked with symbols □, and ○, respectively.

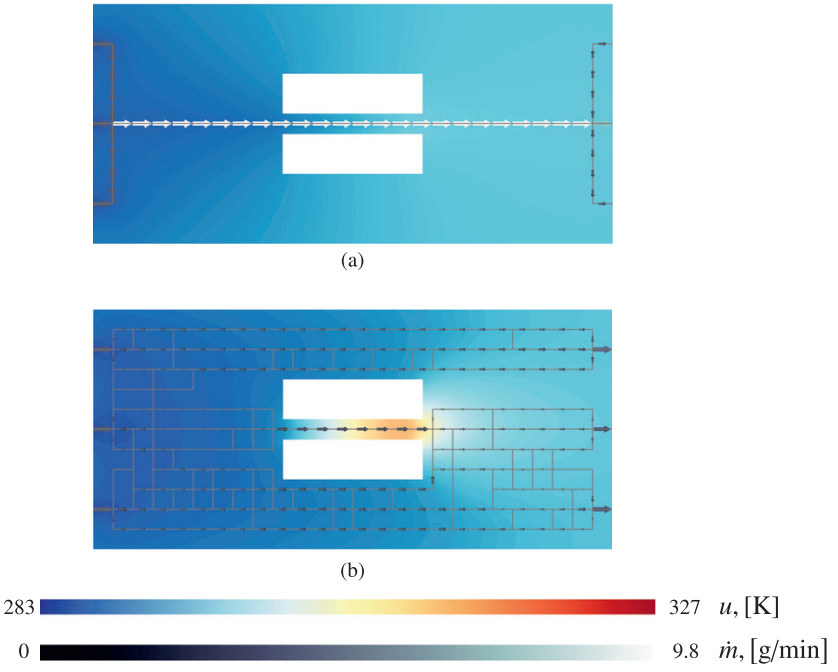

Fig. 7. Selected individuals at generation $t = 2000$ for the uniform heat trap with constant inflow: (a) candidate solution that minimizes both ϕ_v and ϕ_T; (b) individual that minimizes ϕ_f.

front). This individual is very similar to that shown in Fig. 7(a) for constant inflow, except for the fact that the flow is led through channels in the upper part of the domain and therefore has little effect on reducing the maximum temperature. With respect to the void volume fraction objective function, both networks are equivalent. Let us now focus on the tight branch with lower values of ϕ_T. Contrary to the constant inflow rate case, individuals with increasing value of ϕ_v and decreasing value of ϕ_f have a lower value of ϕ_T. Thus, the individual that minimizes ϕ_T is located at the opposite end of the branch, compared to the result for the constant inflow case. This individual, denoted by (b) on the front and marked with a □ symbol, is shown in Fig. 9(b). As for constant inflow, the flow is collected into a set of channels passing through the central strip where the heat source is applied. However, this time a dense network is created before and after the central strip to

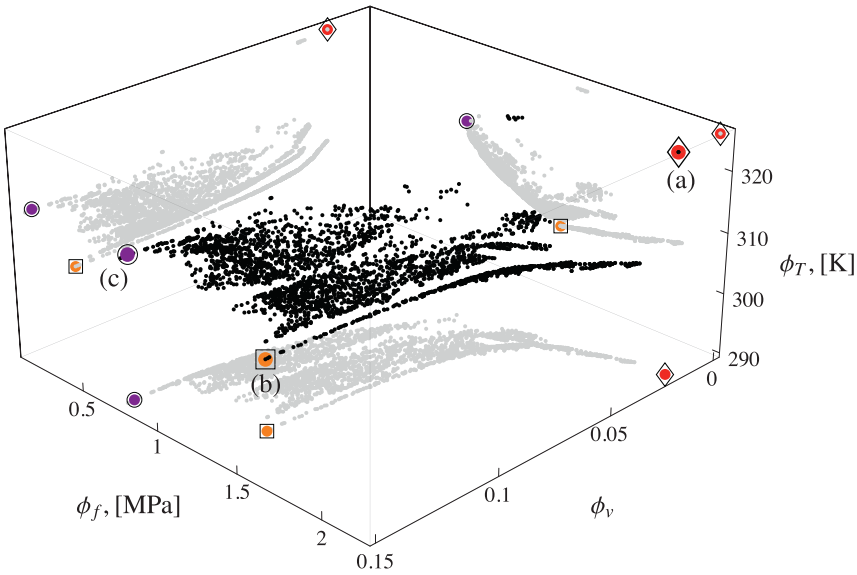

Fig. 8. Pareto-optimal front after 4000 generations of the genetic algorithm considering constant power in the uniform heat trap example. Selected candidate solutions in the front correspond to those shown in Fig. 9(a), (b) and (c), marked with symbols ◇, □ and ○, respectively.

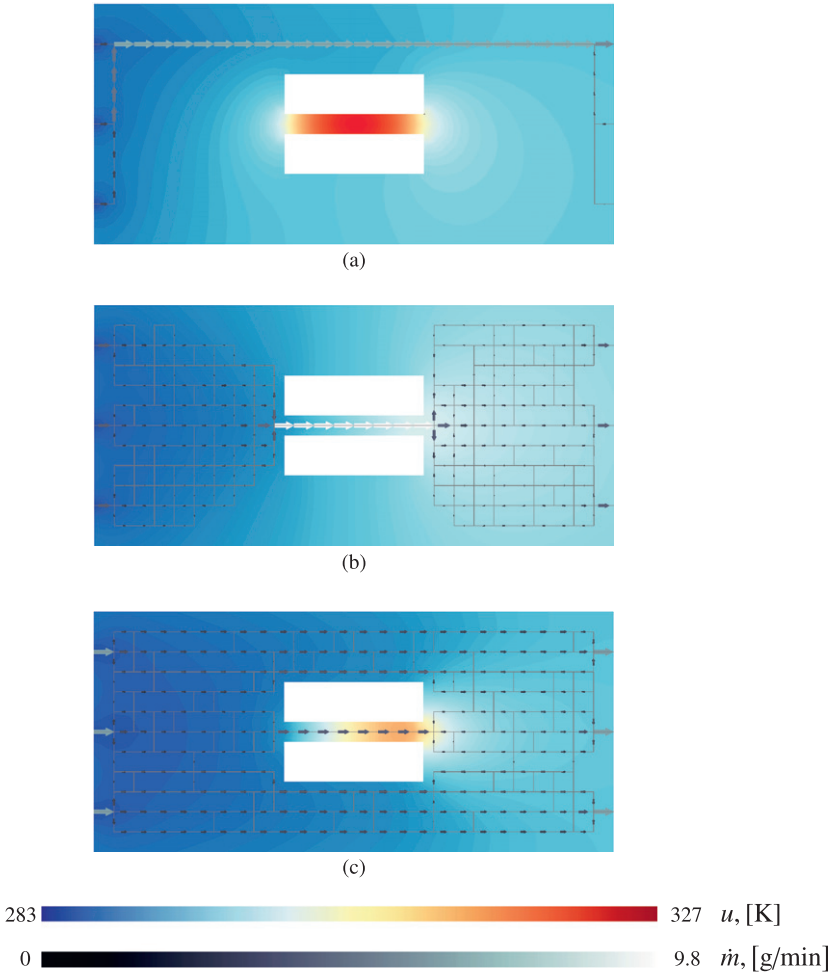

Fig. 9. Selected individuals for the uniform heat trap example with constant power at generation $t = 4000$, minimizing: (a) ϕ_v; (b) ϕ_T; and (c) ϕ_f.

minimize the pressure drop in these regions. This individual contains the maximum value of the flow, which is roughly half of that for constant inflow. When considering constant power, the flow in the microchannels is reduced and therefore the maximum temperature increases. As a result, there is a difference of almost 7 K between this individual and the one displayed in Fig. 7(a). Yet another branch of the front contains individuals with high flow efficiency. The individual that minimizes the pressure drop, labeled (c) in the front and marked with a ○ symbol, is shown in Fig. 9(c). This individual is very similar to the one shown in Fig. 7(b).

6.2. Localized heating example

Consider a rectangular domain $\Omega = (35 \times 20)\,\mathrm{mm}^2$. For this 2D optimization problem, the microvascular network template contains 1241 microchannels (Fig. 10(a)). There is a single inflow and a single outflow, located on the center of left and right edges, respectively. Flow boundary conditions include a prescribed mass inflow $\dot{m}_S = 10$ g/min of water and zero pressure at the outflow. For the thermal boundary value problem, all edges have a convective boundary condition and two

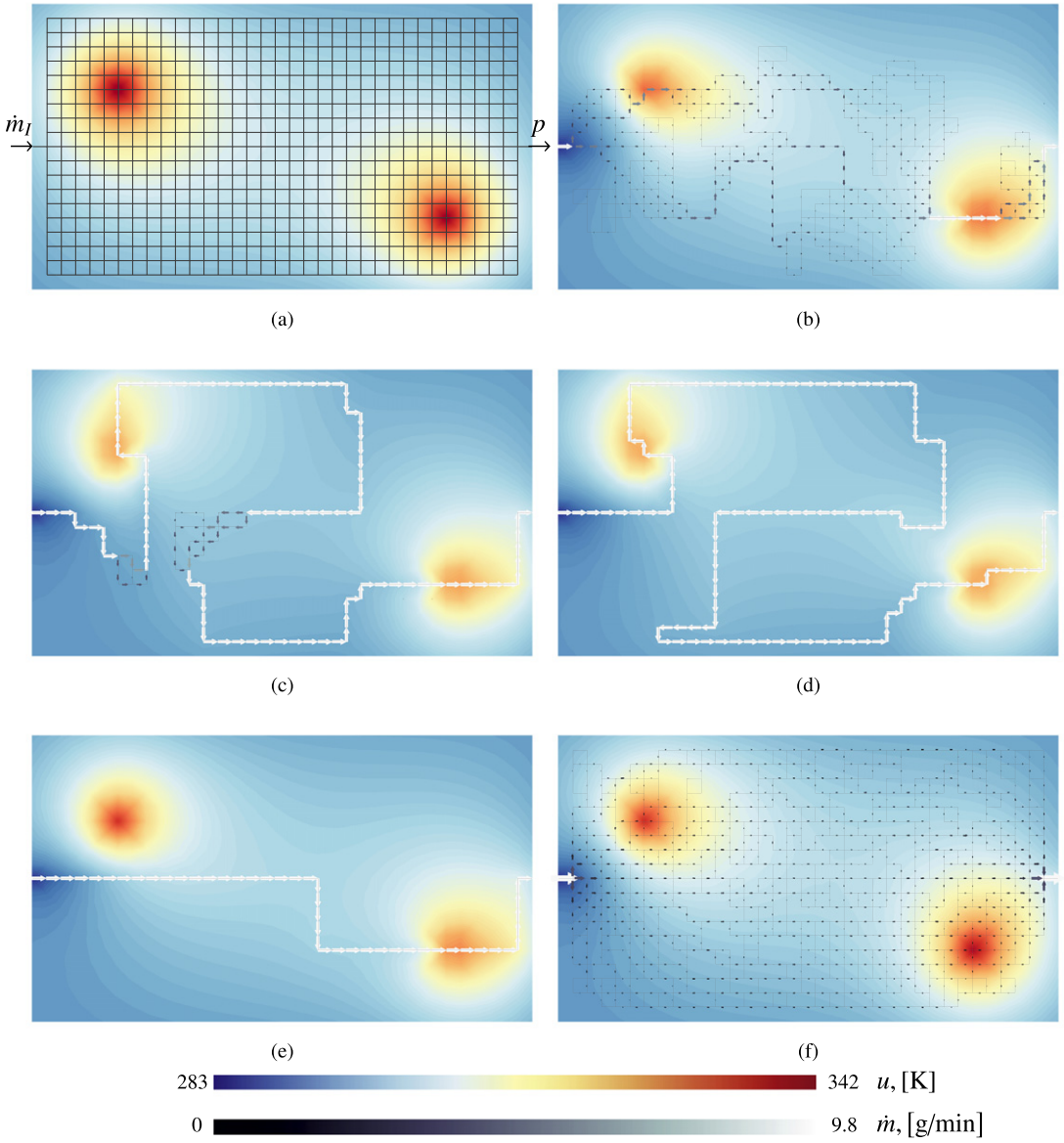

Fig. 10. Results for the localized heat source example for constant inflow. (a) Microvascular network template for this problem with 1241 channels and temperature solution without flow. (b), (c) and (d) show the individuals that minimize ϕ_T at generations $t = 100$, $t = 1000$ and $t = 10{,}000$, respectively. (e) and (f) represent the solutions that minimize ϕ_v and ϕ_f at generation $t = 10{,}000$, respectively. Arrows are sized proportionally to the flow magnitude.

localized heat sources are applied, as indicated in Fig. 10(a). Also, the inlet temperature of the fluid is set at $u_f = 283.15$ K. The temperature distribution obtained using a finite element discretization in the absence of flow is also shown in Fig. 10(a), where a temperature difference of 59 K is observed. The diameter set considered in the optimization is $\mathcal{D}[\mu m] = \{0, 150\}$. As in the previous example, results are reported for constant mass inflow and for constant power. For the latter, the inflow is scaled such that the power of the candidate solutions equals that of the template configuration.

6.2.1. Constant inflow results

Fig. 10 also reports candidate solutions obtained throughout the evolution of the genetic algorithm. Fig. 10(b), (c) and (d) represent the evolution of the candidate solution that minimizes the value of ϕ_T at generations $t = 100$, $t = 1000$ and $t = 10{,}000$, respectively. It can be seen that the topology of the individual converges to a single path of interconnected microchannels going through the hot spots. Also, after reaching the first hot spot, the topology of the network is configured in such a way that the flow is taken over the cooler areas of the domain, allowing for the fluid to release some of its thermal energy. For the individual shown in Fig. 10(d), the maximum temperature is reduced by approximately 18 K. Due to its structure, it is expected that this solution has a poor performance for the flow efficiency objective function. Fig. 10(e) and (f) also show optimal solutions at generation $t = 10{,}000$. The individual presented in Fig. 10(e) minimizes the void volume fraction, as it does its best to connect the inflow and outflow locations with a straight path of microchannels. The individual shown in Fig. 10(f) maximizes the flow efficiency, as it divides the flow in as many channels as possible to the cost of increasing the void volume fraction.

Fig. 11 presents the entire Pareto-optimal front for this problem at generation $t = 10{,}000$. The front is again projected onto three orthogonal planes to assist with the visualization. The projection on the (ϕ_f, ϕ_T) plane is very well defined, and there is a large range of individuals for which the maximum temperature objective ϕ_T remains almost constant. This compares similarly with the front obtained for constant inflow presented in Section 6.1. The same symbols as before are used, so Fig. 10(d), (e) and (f) are marked with □, ◇, and ○ symbols, respectively. The objective function ranges for the front are: ϕ_v [%]: (0.96, 20], ϕ_f [MPa]: (0.08, 1.7) and ϕ_T [K]: [324.2, 342.2].

6.2.2. Constant power results

Three candidate solutions at generation $t = 10{,}000$ for the localized heat source considering constant power are illustrated in Fig. 12. The genetic algorithm is able to capture the individual with the least possible void volume fraction in Fig. 12(a). The candidate solution presented in Fig. 12(b) minimizes the value of ϕ_T. As in the case for constant inflow rate, the flow is directed to the hot spots, but this time with a dense network to reduce the amount of energy needed to drive the flow. It is worth mentioning that the entire flow is collected when reaching the second hot spot. However, since collecting the flow in a single path increases the pressure drop rapidly, the flow is only collected in a couple of microchannels. Finally, the individual outlined in Fig. 12(c) minimizes the pressure drop, and it has a structure that again resembles that of the microvascular network template.

The front in this case, shown in Fig. 13, follows the same pattern as that of the previous example for constant power. It is clearly more segregated than the front shown in Fig. 11. Once again, the individual that minimizes ϕ_T is located at the oppo-

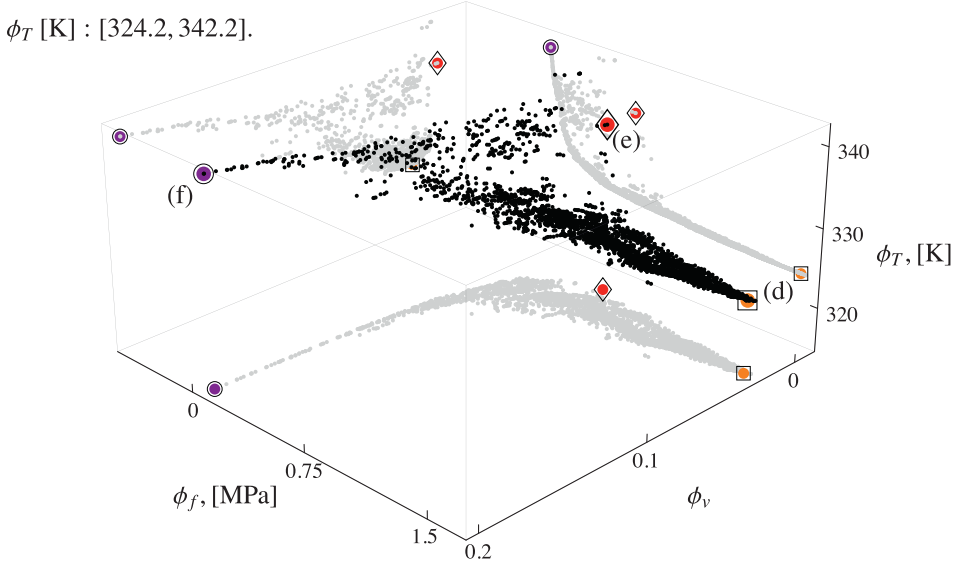

Fig. 11. Pareto-optimal front after 10,000 generations of the NSGA-II for the localized heat example with constant inflow. Selected candidate solutions in the front, marked with □, ◇, and ○ symbols, correspond to those shown in Fig. 10(d), (e), and (f), respectively.

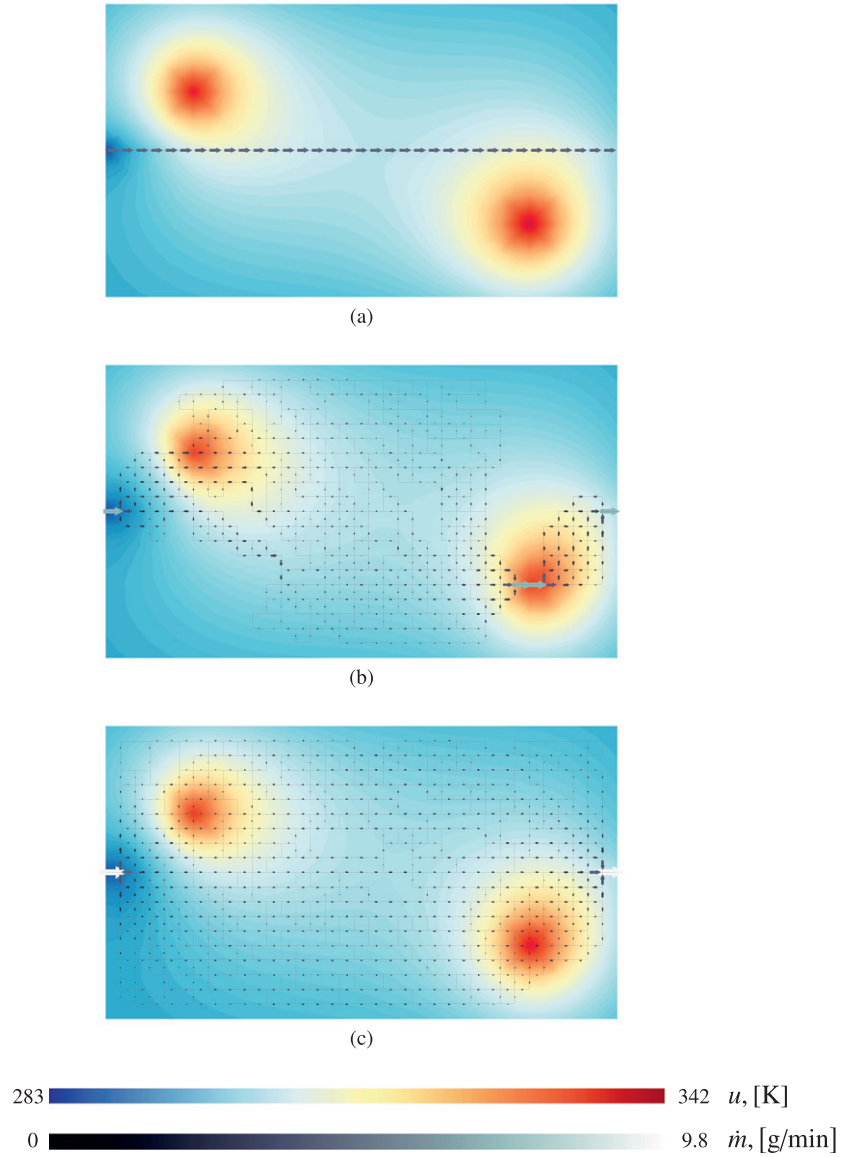

Fig. 12. Selected individuals at generation t = 10,000 considering constant power for the localized heat source example. Labels (a), (b), and (c), respectively, denote optimal solutions with respect to the ϕ_v, ϕ_T, and ϕ_f objective functions.

site end from that for constant inflow, for the set of individuals with low value of ϕ_T. This individual, labeled (b) on the front and marked with a □ symbol, corresponds to Fig. 12(b). It can be clearly seen in the $\phi_f - \phi_T$ plane that candidate solutions increase the value of ϕ_T as the pressure increases. Again, this is due to the fact that, as the network is less flow efficient, the flow decreases to keep the power constant, reducing also its ability to remove heat from the domain. The other two marked individuals on the front correspond to Fig. 12(a) and (c), and are marked with ♢ and ○ symbols, respectively. The reported ranges for objective functions are: ϕ_v [%]: (0.75, 22), ϕ_f [MPa]: (0.072, 0.22) and ϕ_T [K]: [335.9, 343.5]. As it was the case for the previous example, the pressure range is drastically improved, to the cost of incrementing the temperature range. The upper bound on the pressure considering constant power is 13% of that for constant inflow, and there is a difference of almost 12 K between the lower bounds for the temperature.

A direct comparison between the thermal results presented in Figs. 10(d) and 12(b) does not however account for the very large pressure penalty associated with the single channel solution obtained with the constant inflow case (Fig. 10(d)). If indeed we scale down the driving pressure for that case to match the reference power value, the corresponding temperature drop would only amount to 0.3 K.

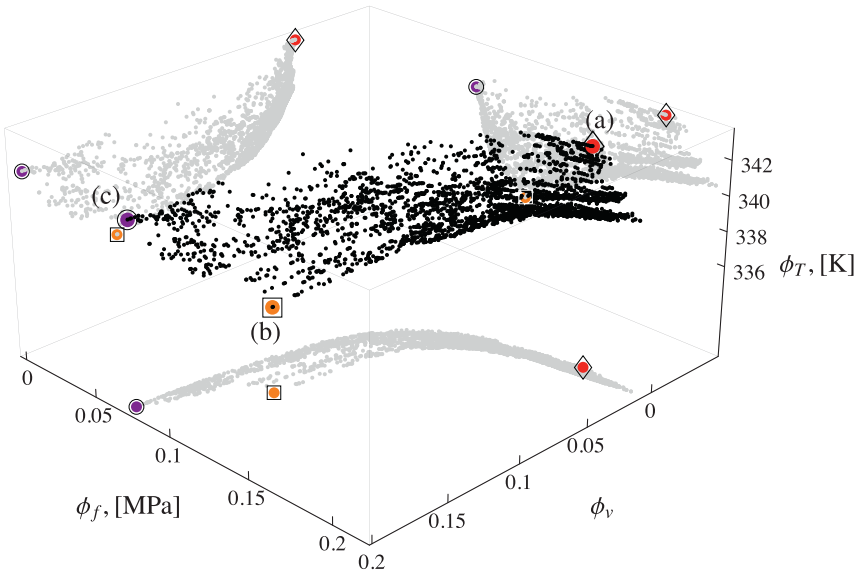

Fig. 13. Pareto-optimal front for the localized heat example with constant power at generation t = 10,000. Selected candidate solutions, labeled (a), (b), and (c) in the optimal front, correspond to the individuals presented in Figs. 12(a), (b) and (c). These solutions are also marked with ♢, □, and ○ symbols, respectively.

6.3. Microvascular fin

Consider the same domain studied in the previous problem, i.e. $\Omega = (35 \times 20)\ \text{mm}^2$, the same microvascular network template, and the same diameter set for the optimization. As in the previous example, flow boundary conditions include a single mass inflow of water $\dot{m}_S = 10\ \text{g/min}$ and zero pressure at a single outflow. This problem is studied in two separate cases, depending on how the flow boundary conditions are placed in the domain. The first scenario follows the previous example, placing the inflow and outflow on opposite sides of the domain. The second scenario places the flow boundary conditions on the same edge of the domain. Only constant inflow results are reported for both cases. For the thermal boundary value problem, the ambient temperature for this optimization problem is u_∞ = 363.15 K, thus the specimen is placed in a hot environment. As before, the inlet temperature of the fluid is set at u_f = 283.15 K. For this optimization, energy is lost through the surface of the specimen only. Thus, convection through the surface is taken into account by having a temperature-dependent heat source $f = h_f(u_\infty - u)$, as explained in Section 3.3. The edges in this example are insulated, i.e. $\bar{q} = 0$. Thus, in the absence of flow, the temperature of the entire domain equals that of the environment. The optimization problem is stated as:

$$\begin{aligned}&\text{maximize } \Phi_1 = \{\phi_s\},\\ &\text{and minimize } \Phi_2 = \{\phi_v, \phi_f\},\\ &\text{such that } \psi_c = 0,\end{aligned}$$

with ϕ_s defined in Eq. 14. In other words, the thermal optimization problem investigated in this application consists in designing the embedded network to achieve optimal heat exchange between the microvascular fin and its surrounding.

6.3.1. Flow boundary conditions on opposite sides

The Pareto-optimal surface for this case is given in Fig. 14. For this problem, the surface convected energy objective function ϕ_s is maximized, thus the Pareto-optimal front has a different configuration when compared with the fronts of previous problems. Moreover, this front contains a feature that is particularly different, for the candidate solution that minimizes the void volume fraction objective function, labeled (a) in the front, is an inflection point for the ϕ_s objective function. Starting from this individual, solutions with increasing values of ϕ_f create a trail of individuals that have increasingly higher values of ϕ_s. The solution located at the extremum of this trail, even though not being optimal in any of the objective functions, has also been selected for visualization to explain this particular feature of the front.

Fig. 15 presents the selected candidate solutions for this problem. The individuals that minimize ϕ_v and ϕ_f, shown in Fig. 15(a) and (b), have similar features as those shown in the previous problems. These figures are labeled (a) and (b) in the Pareto-optimal front of Fig. 14, and are marked with ♢ and ○ symbols, respectively. The solution presented in Fig. 15(c), labeled (c) in the front and marked with a □ symbol, maximizes the surface convected energy objective function ϕ_s. Therefore, this individual maximizes the difference $u^h - u_\infty$ over the entire domain Ω^h, and because u_∞ is constant, this means that the temperature is minimized on average over the domain. A similar solution would thus be obtained by

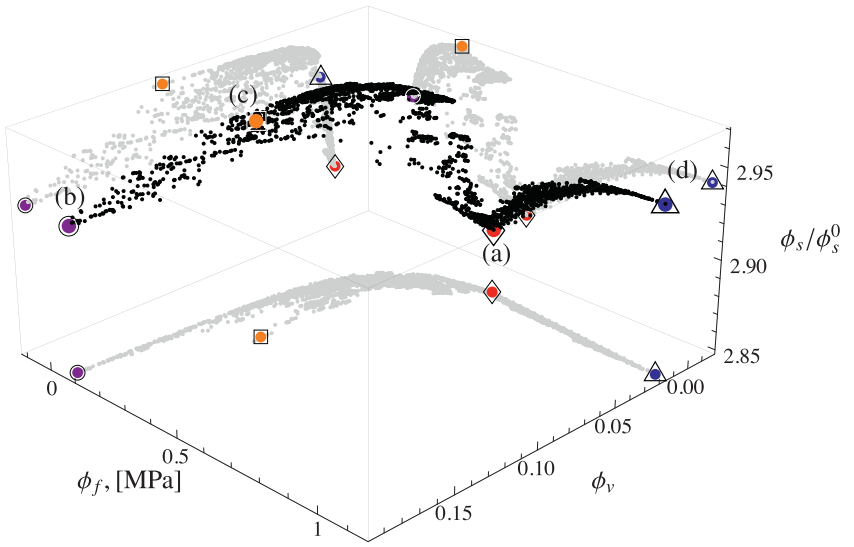

Fig. 14. NSGA-II results at generation $t = 10{,}000$ for the fin specimen example with flow boundary conditions on opposite sides of the domain. Selected candidate solutions, labeled in the front and marked with ◇, ○, □, and △ symbols, are illustrated in Fig. 15.

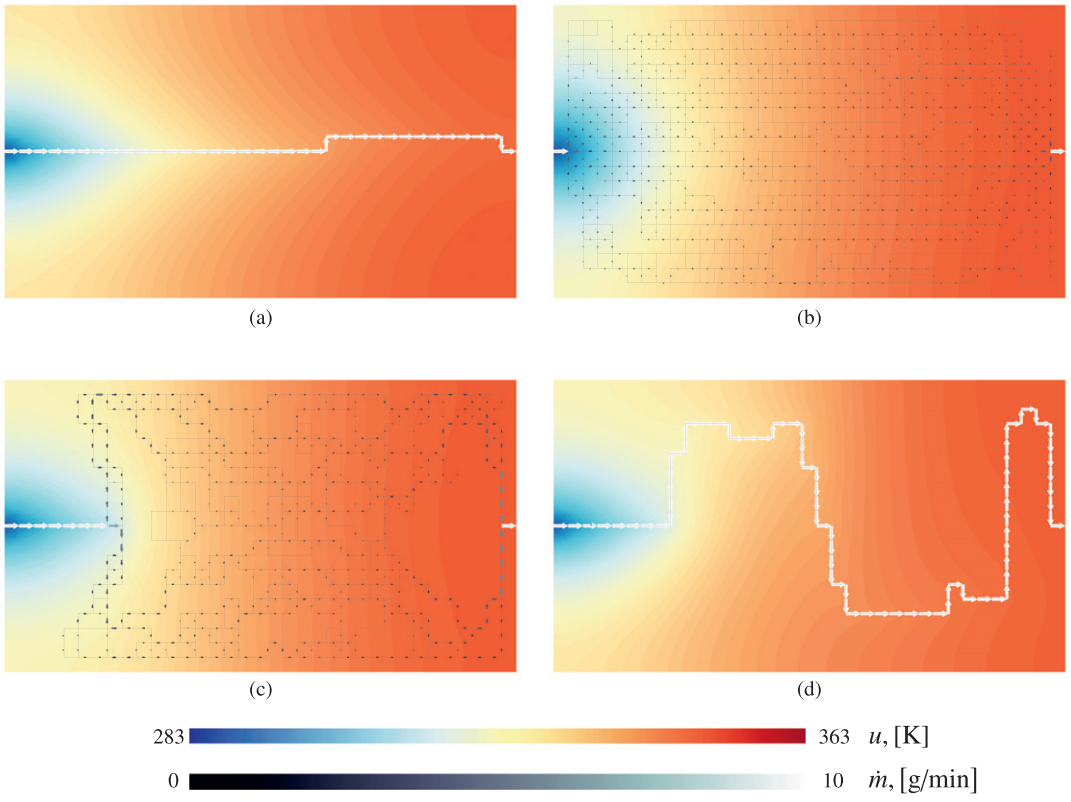

Fig. 15. Selected candidate solutions for the fin example considering constant inflow and flow boundary conditions on opposite sides of the domain. (a) and (b) correspond to the candidate solutions that minimize ϕ_v and ϕ_f, respectively. (c) corresponds to the individual that maximizes ϕ_s. Finally, the individual illustrated in (d) is displayed to explain the trail in the Pareto-optimal surface of Fig. 14.

considering the average temperature of the domain as an objective function, instead of using the defined objective function ϕ_s. The microvascular network for this solution roughly distributes the flow evenly through the surface of the specimen. First, the network halves the flow and channels it to the top and bottom edges of the specimen. Then, part of the flow remains in

these edges, while the rest is channeled back to the center of the specimen. Near the outflow, the flow is collected again near the top and bottom edges in two halves before exiting the domain. The last solution shown in Fig. 15(d) is presented to ex-

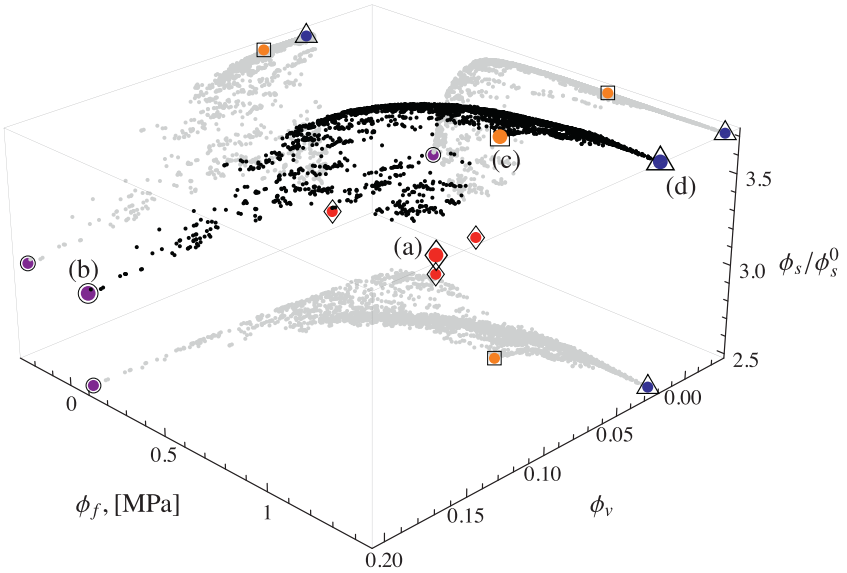

Fig. 16. Pareto-optimal surface at generation t = 10,000 for the fin specimen example with the inflow and outflow located on the same edge. Individuals selected for visualization are displayed in Fig. 17 and are labeled in the front and marked with symbols ◇, ○, □, and △ symbols.

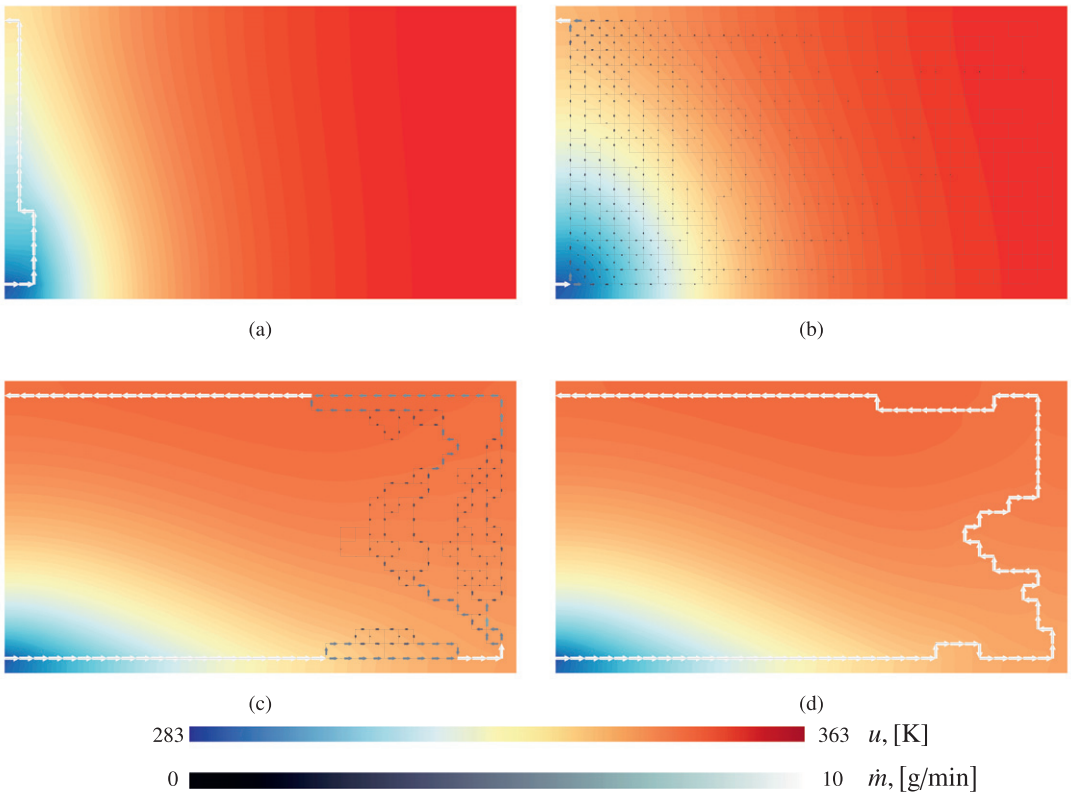

Fig. 17. Selected individuals taken from the Pareto-optimal front of Fig. 16 for the microvascular fin example with the inflow and outflow located on the same edge of the domain. As before, (a) and (b) minimize objective functions ϕ_v and ϕ_f, respectively. (c) and (d) show candidate solutions with a high value of ϕ_s.

plain the trail in the Pareto-optimal surface shown in Fig. 14, a feature that was not present in the previous optimization examples. This individual is marked with a △symbol and is labeled (d) on the front. The individual shows that, starting from the individual with minimum void volume fraction, better configurations for the convected surface energy can be obtained with networks that collect the flow into a single set of interconnected microchannels. Increasing the length of these single-path networks increases the pressure drop, as determined by Eq. 2, and thus reduces the flow efficiency. However, the flow is exposed to more surface area, which has the effect of reducing the temperature more efficiently and thus increasing the difference $u^h - u_\infty$ over Ω^h. This serpentine-like topology therefore seems to be a good candidate solution for minimizing the temperature of the domain, to the cost of decreasing the flow efficiency. Note however, that this solution is worse than that shown in Fig. 15(c) with respect to ϕ_s.

6.3.2. Flow boundary conditions on the same side

For this last optimization problem, the inflow and outflow are located on the left edge of the domain. Again, after 10,000 generations, the Pareto-optimal surface for this problem is well established, as displayed in Fig. 16. Once more, the selected individuals marked on the front are displayed in Fig. 17. Fig. 17(a) and (b) follow the same structure as the corresponding solutions in previous optimizations. The solution illustrated in Fig. 17(c) maximizes the value of the objective function ϕ_s. The flow is entirely collected close to the inflow and outflow locations. Close to the right edge, the flow is divided in many paths, thus reducing the pressure drop in this region. The last figure shows the individual with the worst value of the flow efficiency objective function. This individual has a similar structure than the one shown in Fig. 17(c) close to inlet and outlet locations. However, because the flow is collected into a single path of channels, the pressure drop is increased dramatically. Still, this individual is optimal for the surface convected energy objective function ϕ_s.

7. Conclusions

This work has presented a multi-objective constrained optimization framework for the design of microvascular networks for active cooling applications. The scheme is able to accurately define Pareto-optimal fronts for the objective functions considered, thus capturing the trade-offs between competing objectives for a final design decision. The algorithm can be used with an arbitrary number of objective functions and constraints. It was shown how coupling a finite element PDE solver with the multi-objective constrained genetic algorithm provides a powerful tool for multi-physics optimization. It is worth mentioning that even though extreme individuals on the Pareto-optimal fronts have been reported, the entire front is available to the analyst for a final decision.

The initial population usually contains only unfeasible individuals, but the population becomes feasible after only a few generations. There is a considerable difference between the evaluation times of feasible and unfeasible individuals. Strictly speaking, unfeasible individuals are not even evaluated, their objective functions are penalized with very high values. This difference in evaluation times requires a very efficient parallel implementation, that takes into account the load balancing on processors to achieve optimal speed-ups.

Acknowledgments

The authors gratefully acknowledge support from AFOSR (MURI Grant No. F49550-05-1-0346) and thank Prof. Arne J. Pearlstein from the Mechanical Science and Engineering Department at the University of Illinois for providing valuable insight on the convective heat transfer problems.

References

[1] H. Hensel, Heat and cold, Annual Review of Physiology 21 (1) (1959) 91–116, doi:10.1146/annurev.ph.21.030159.000515. <http://arjournals.annualreviews.org/doi/abs/10.1146/annurev.ph.21.030159.000515>.
[2] K.R. Morgareidge, F.N. White, Cutaneous vascular changes during heating and cooling in the galapagos marine iguana, Nature 223 (1969) 587–591. <http://dx.doi.org/10.1038/223587a0>.
[3] F. Seebacher, C.E. Franklin, Integration of autonomic and local mechanisms in regulating cardiovascular responses to heating and cooling in a reptile (crocodylus porosus), Journal of Comparative Physiology B: Biochemical, Systemic, and Environmental Physiology 174 (7) (2004) 577–585. <http://dx.doi.org/10.1007/s00360-004-0446-0>.
[4] T. Cooper, W.C. Randall, A.B. Hertzman, Vascular convection of heat from active muscle to overlying skin, Journal of Applied Physiology 14 (2) (1959) 207–211. <http://jap.physiology.org/cgi/reprint/14/2/207.pdf>, <http://jap.physiology.org/cgi/content/abstract/14/2/207>.
[5] G. Brengelmann, Specialized brain cooling in humans?, FASEB Journal 7 (12) (1993) 1148–1152 <http://www.fasebj.org/cgi/reprint/7/12/1148.pdf>, <http://www.fasebj.org/cgi/content/abstract/7/12/1148>.
[6] Y. Bar-Cohen, Biomimetics – using nature to inspire human innovation, Bioinspiration and Biomimetics 1 (1) (2006) P1. <http://dx.doi.org/10.1088/1748-3182/1/1/P01>.
[7] P. Fratzl, Biomimetic materials research: what can we really learn from nature's structural materials?, Journal of The Royal Society Interface 4 (15) (2007) 637–642 <http://rsif.royalsocietypublishing.org/content/4/15/637.full.pdf+html>, doi:10.1098/rsif.2007.0218, <http://dx.doi.org/10.1098/rsif.2007.0218>.
[8] B. Bhushan, Biomimetics: lessons from nature – an overview, Philosophical Transactions of the Royal Society A: Mathematical, Physical and Engineering Sciences 367 (1893) (2009) 1445–1486. <http://rsta.royalsocietypublishing.org/content/367/1893/1445.full.pdf+html>, doi:10.1098/rsta.2009.0011, <http://dx.doi.org/10.1098/rsta.2009.0011>.
[9] J.F.V. Vincent, Biomimetics – a review, in: Proceedings of the Institution of Mechanical Engineers, Part H, Journal of Engineering in Medicine 223.
[10] D. Therriault, S.R. White, J.A. Lewis, Chaotic mixing in three-dimensional microvascular networks fabricated by direct-write assembly, Nature Materials 2 (4) (2003) 265–271. <http://dx.doi.org/10.1038/nmat863>.

[11] K.S. Toohey, N.R. Sottos, J.A. Lewis, J.S. Moore, S.R. White, Self-healing materials with microvascular networks, Nature Materials 6 (8) (2007) 581–585. <http://dx.doi.org/10.1038/nmat1934>.
[12] B.D. Kozola, L.A. Shipton, V.K. Natrajan, K.T. Christensen, S.R. White, Characterization of active cooling and flow distribution in microvascular polymers, Journal of Intelligent Material Systems and Structures. <http://dx.doi.org/10.1177/1045389X10379662>
[13] D. Tuckerman, R. Pease, High-performance heat sinking for vlsi, Electron Device Letters 2 (5) (1981) 126–129.
[14] A. Weisberg, H.H. Bau, J. Zemel, Analysis of microchannels for integrated cooling, International Journal of Heat and Mass Transfer 35 (10) (1992) 2465–2474. doi:10.1016/0017-9310(92)90089-B, <http://dx.doi.org/10.1016/0017-9310(92)90089-B>.
[15] X. Wei, Y. Joshi, M.K. Patterson, Experimental and numerical study of a stacked microchannel heat sink for liquid cooling of microelectronic devices, Journal of Heat Transfer 129 (10) (2007) 1432–1444. doi:10.1115/1.2754781, <http://link.aip.org/link/?JHR/129/1432/1>.
[16] P. Wu, W.A. Little, Measurement of the heat transfer characteristics of gas flow in fine channel heat exchangers used for microminiature refrigerators, Cryogenics 24 (8) (1984) 415–420. doi:10.1016/0011-2275(84)90015-8, <http://www.sciencedirect.com/science/article/B6TWR-48HY7GT-XY/2/2bcd94912b65a130c352fd0bdf205f9e>.
[17] A. Bejan, S. Lorente, Constructal theory of generation of configuration in nature and engineering, Journal of Applied Physics 100 (4) (2006) 041301. <http://dx.doi.org/10.1063/1.2221896>.
[18] A. Bejan, S. Lorente, K.-M. Wang, Networks of channels for self-healing composite materials, Journal of Applied Physics 100 (3) (2006) 033528. doi:10.1063/1.2218768, <http://dx.doi.org/10.1063/1.2218768>.
[19] A. Bejan, S. Lorente, Design with Constructal Theory, John Wiley & Sons Inc., 2008.
[20] J. Lee, S. Lorente, A. Bejan, Transient cooling response of smart vascular materials for self-cooling, Journal of Applied Physics 105 (6) (2009) 064904. doi:10.1063/1.3068323, <http://link.aip.org/link/?JAP/105/064904/1>.
[21] K.-M. Wang, S. Lorente, A. Bejan, Vascular materials cooled with grids and radial channels, International Journal of Heat and Mass Transfer 52 (5–6) (2009) 1230–1239. doi:10.1016/j.ijheatmasstransfer.2008.08.027, <http://dx.doi.org/10.1016/j.ijheatmasstransfer.2008.08.027>.
[22] K.-M. Wang, S. Lorente, A. Bejan, Vascular structures for volumetric cooling and mechanical strength, Journal of Applied Physics 107 (4) (2010) 044901. doi:10.1063/1.3294697, <http://link.aip.org/link/?JAP/107/044901/1>.
[23] T. Borrvall, A. Klarbring, J. Petersson, B. Torstenfelt, Topology optimization in fluid mechanics, in: Fifth World Congress on Computational Mechanics, Vienna, Austria, 2002.
[24] T. Borrvall, J. Petersson, Topology optimization of fluids in stokes flow, International Journal for Numerical Methods in Fluids 41 (1) (2003) 77–107. doi:10.1002/fld.426, <http://dx.doi.org/10.1002/fld.426>.
[25] A. Klarbring, J. Petersson, B. Torstenfelt, M. Karlsson, Topology optimization of flow networks, Computer Methods in Applied Mechanics and Engineering 192 (35–36) (2003) 3909–3932. <http://dx.doi.org/10.1016/S0045-7825(03)00393-1>.
[26] D.E. Goldberg, Genetic Algorithms in Search, Optimization, and Machine Learning, Addison-Wesley Publishing Company, Massachusetts, 1989.
[27] D.E. Goldberg, The Design of Innovation: Lessons from and for Competent Genetic Algorithms, Kluwer Academic Publishers, Massachusetts, 2002.
[28] Z. Michalewicz, D. Dasgupta, R.G.L. Riche, M. Schoenauer, Evolutionary algorithms for constrained engineering problems, Computers and Industrial Engineering 30 (4) (1996) 851–870. <http://dx.doi.org/10.1016/0360-8352(96)00037-X>.
[29] E. Zitzler, L. Thiele, Multiobjective evolutionary algorithms: a comparative case study and the strength pareto approach, IEEE Transactions on Evolutionary Computation 3 (4) (1999) 257–271. <http://dx.doi.org/10.1109/4235.797969>.
[30] I. Sbalzarini, S. Muller, P. Koumoutsakos, Microchannel optimization using multiobjective evolution strategies;;, in: E. Zitzler, L. Thiele, K. Deb, C. Coello Coello, D. Corne (Eds.), Evolutionary Multi-Criterion Optimization of Lecture Notes in Computer Science, vol. 1993, Springer, Berlin, Heidelberg, 2001, pp. 516–530. <http://dx.doi.org/10.1007/3-540-44719-9_36>.
[31] K. Deb, A. Pratap, S. Agarwal, T. Meyarivan, A fast and elitist multiobjective genetic algorithm: NSGA-II, IEEE Transactions on Evolutionary Computation 6 (2) (2002) 182–197. <http://dx.doi.org/10.1109/4235.996017>.
[32] A.M. Aragón, J.K. Wayer, P.H. Geubelle, D.E. Goldberg, S.R. White, Design of microvascular flow networks using multi-objective genetic algorithms, Computer Methods in Applied Mechanics and Engineering 197 (49–50) (2008) 4399–4410. <http://dx.doi.org/10.1016/j.cma.2008.05.025>.
[33] D. Therriault, R. Shepherd, S. White, J. Lewis, Fugitive inks for direct-write assembly of three-dimensional microvascular networks, Advanced Materials 17 (4) (2005) 395–399. <http://dx.doi.org/10.1002/adma.200400481>.
[34] V. Natrajan, K. Christensen, Microscopic particle image velocimetry measurements of transition to turbulence in microscale capillaries, Experiments in Fluids 43 (1) (2007) 1–16. <http://dx.doi.org/10.1007/s00348-007-0301-7>.
[35] H.L. Langhaar, Steady flow in the transition length of a straight tube, Journal of Applied Mechanics 9 (1942) A55–A58.
[36] C.A. Brebbia, A.J. Ferrante, Computational Hydraulics, Butterworth Heinemann Ltd., London, 1983.
[37] W.M. Kays, M.E. Crawford, B. Weigand, Convective Heat and Mass Transfer, fourth ed., McGraw-Hill, 2004.
[38] A.M. Aragón, C.A. Duarte, P.H. Geubelle, Generalized finite element enrichment functions for discontinuous gradient fields, International Journal for Numerical Methods in Engineering 82 (2) (2010) 242–268. <http://dx.doi.org/10.1002/nme.2772>.
[39] T. Belytschko, R. Gracie, G. Ventura, A review of extended/generalized finite element methods for material modeling, Modelling and Simulation in Materials Science and Engineering 17 (4) (2009) 043001. <http://stacks.iop.org/0965-0393/17/i=4/a=043001>.
[40] V. Pareto, Manuale di Economia Politica, Piccola Biblioteca Scientifica, Milan, 1906 (Translated into English by Ann S. Schwier, Manual of Political Economy, MacMillan, London, 1971).
[41] E. Cantú-Paz, D.E. Goldberg, Efficient parallel genetic algorithms: theory and practice, Computer Methods in Applied Mechanics and Engineering 186 (2-4) (2000) 221–238. <http://dx.doi.org/10.1016/S0045-7825(99)00385-0>.